# *A model for fibrous illite nucleation and growth in sandstones*

**Robert H. Lander and Linda M. Bonnell**

## ABSTRACT

We have developed a model for the formation of fibrous illite in sandstones where kaolinite is a primary reactant and potassium is derived from in-situ K-feldspar grain dissolution or imported into the model reference frame. Illite fiber nucleation and growth are modeled using Arrhenius expressions that consider saturation state in addition to temperature and time. Nucleation occurs on pore walls, and muscovite and detrital illite may be defined as energetically favorable substrates. The model is integrated with other Touchstone™ models to account for the influence of other diagenetic processes on surface area and reactant volumes and to provide input for permeability simulations.

We evaluated the illite model performance on two data sets: (1) Jurassic quartzose samples from offshore mid-Norway with maximum temperatures ranging from 108 to 173°C (226 to 343°F) and (2) Miocene lithic samples from offshore Southeast Asia that have maximum temperatures ranging from 157 to 182°C (315 to 360°F). The model matches measured abundances of illite, kaolinite, and K-feldspar in both data sets using identical kinetic parameters. Predicted K-Ar ages are consistent with available data given uncertainties associated with detrital contaminants. Although no illite particle-size data are available from the analyzed samples, modeled crystallite thicknesses from the Norway data set are comparable to published measurements of 0.004 to 0.012 $\mu$m from North Sea samples with similar temperature histories.



Manuscript received July 11, 2009; provisional acceptance October 26, 2009; revised manuscript received March 8, 2010; final acceptance April 21, 2010.
DOI:10.1306/04211009121

## AUTHORS

ROBERT H. LANDER ~ *Geocosm LLC, 3311 San Mateo Drive, Austin, Texas 78738; roblander@geocosm.net*

Rob Lander develops diagenetic models for Geocosm LLC. He obtained his Ph.D. in geology from the University of Illinois in 1991, was a research geologist at Exxon Production Research from 1991 to 1993, and worked for Rogaland Research and Geologica AS from 1993 to 2000. He is also a research fellow at the Bureau of Economic Geology.

LINDA M. BONNELL ~ *Geocosm LLC, 3311 San Mateo Drive, Austin, Texas 78738; lmbonnell@geocosm.net*

Linda Bonnell develops diagenetic models and conducts reservoir quality prediction studies for Geocosm LLC. She received her Ph.D. in geology from the University of Illinois in 1990 and subsequently was a research scientist at Washington University, Rice University, Rogaland Research, and Geologica AS. She is also a research fellow at the Bureau of Economic Geology. Linda was an AAPG Distinguished Lecturer in 2003–2004.

## ACKNOWLEDGEMENTS

This work was funded by Geocosm's Consortium for Quantitative Prediction of Sandstone Reservoir Quality (RQC), which is currently supported by the State of Alaska Department of Natural Resources, Anadarko, BHP-Billiton, BP, Chevron, Cobalt International, ConocoPhillips, Devon, Eni, ExxonMobil, Hess, Instituto Mexicano del Petróleo, Maersk, Petrobras, Saudi Aramco, Shell, Statoil, Total, and Woodside. We thank Thomas Moore, Arthur Trevena, Reed Glasmann, and Marek Kacewicz for providing the natural data sets. Richard Larese, Reed Glasmann, and Arthur Trevena, in particular, provided us with invaluable insights regarding these data sets and controls on illitization in general. Reviews by David Awwiller, Stephen Franks, and Olav Walderhaug helped us improve the article. The AAPG Editor thanks the following reviewers for their work on this article: David N. Awwiller, Stephen G. Franks, and Olav Walderhaug.

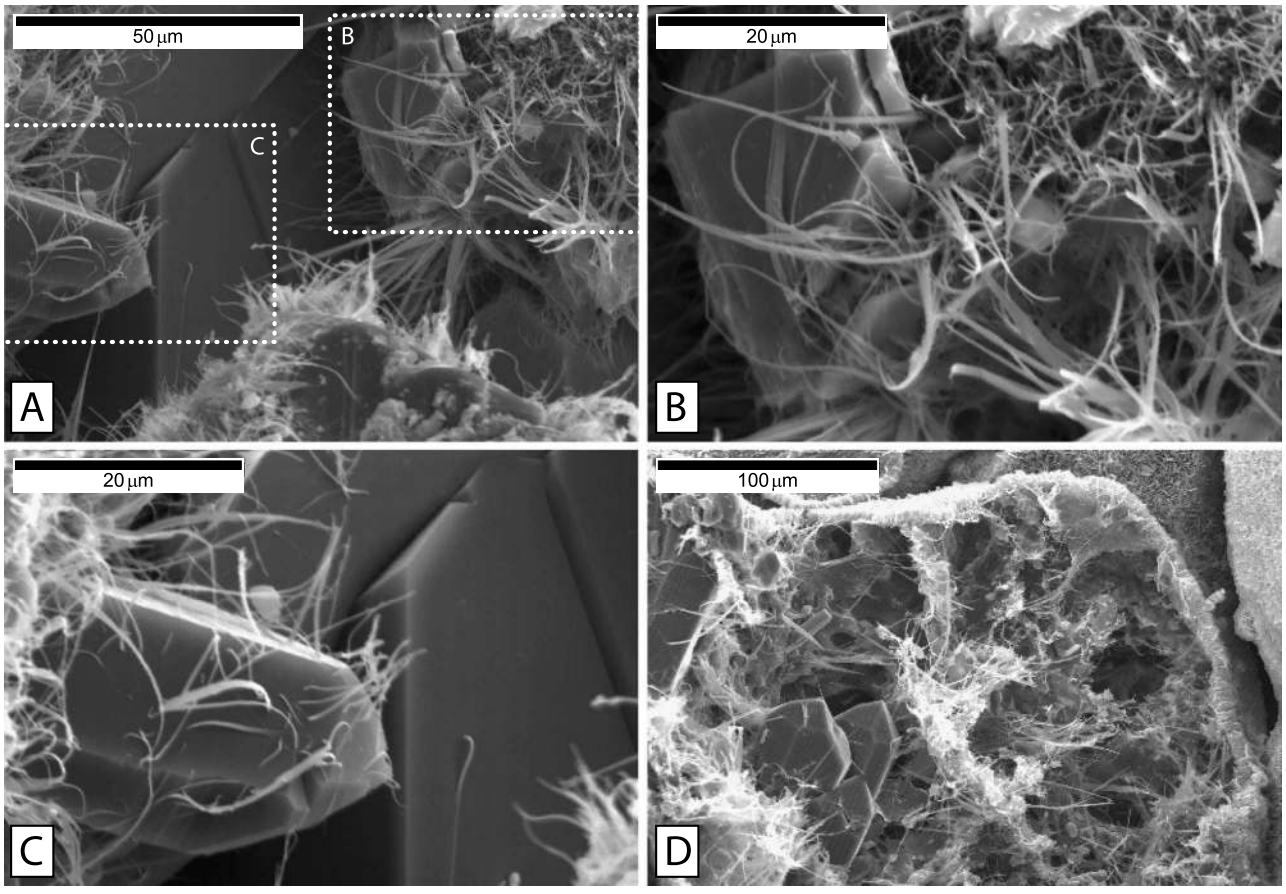


**Figure 1.** Scanning electron microscope photomicrographs illustrating the texture and morphology of fibrous illite in sandstone. (A) Illite fibers growing into an intergranular pore. The white dotted outlines indicate the zoomed-in views shown in panels B and C. (B) Illite fibers typically show a range in sizes, suggesting that the crystallites did not all nucleate simultaneously. (C) Illite fibers appear to have nucleated on authigenic quartz cement. (D) Illite fibers growing into a moldic pore that likely formed in response to dissolution of a feldspar grain.

## INTRODUCTION

Accurate predictive models for the occurrence and properties of fibrous illite would be useful for hydrocarbon exploration and production given that illite can have a severe detrimental effect on reservoir properties. In particular, the high surface area, pore-bridging texture, and significant associated microporosity of illite fibers (Figure 1) act to reduce permeability while increasing irreducible water saturation and capillary entry pressure (McHardy et al., 1982; Kantorowicz, 1984, 1990; Bjørlykke et al., 1986, 1992). Illite fibers generally have thicknesses, widths, and lengths that are on the order of 0.05, 0.5, and 50 $\mu$m, respectively (Figure 1) (Güven et al., 1980; Nagy, 1994; Lanson et al., 1996, 2002). The resulting specific surface areas (areas per solid volume) are at least two orders of magnitude greater than cements such as calcite or quartz that are composed of larger, blockier crystals (Panda and Lake, 1995). Illite fibers tend to grow as independent strands that extend well into the pore space of host sandstones (Figure 1) where they may significantly increase flow-path tortuosity (Stalder, 1973; Pallatt et al., 1984; Cocker, 1986; Panda and Lake, 1995). Because illite fibers frequently extend farther into pores than other authigenic clays, they tend to cause larger permeability reductions for a given bulk volume. Moreover, the higher microporosity of fibrous illite compared to most other authigenic clays (Nadeau and Hurst, 1991) means that a comparable solid volume will invade a larger proportion of macropore volume.

Fibrous illite appears to form mainly by reaction of kaolin minerals and $K^+$. Potassium may be derived from local K-feldspar dissolution (e.g., Bjørlykke et al., 1986, 1992; Bjørkum and Gjelsvik, 1988; Chuhan et al., 2001; Franks and Zwingmann, this issue) or external sources such as migrating fluids (e.g., Robinson et al., 1993; Lanson et al., 1996; De Ros, 1998; Zwingmann et al., 1999) or dissolved solutes from adjacent shales (Gaupp et al., 1993; Berger et al., 1997; Thyne et al., 2001; Clauer et al., 2008). The reaction pathway leading to fibrous illite seems to require higher thermal exposures compared to illite that forms by smectite illitization (Lander et al., 1990; Stroker and Harris, 2009). The rate of the reaction leading to fibrous illite growth, once it begins, appears to be rapid. One line of evidence for this interpretation is the narrow present-day temperature range (120 to 140°C [248 to 284°F]) from incipient to pervasive illitization in Jurassic sandstones of the North Sea and Haltenbanken (e.g., Bjørlykke et al., 1986, 1992, 1995; Ehrenberg and Nadeau, 1989; Glasmann, 1992; Ramm and Ryseth, 1996; Midtbø et al., 2000).

## MODEL FORMULATION

The model simulates the following through geologic time: (1) the kinetics of illite crystal nucleation and growth by considering saturation state, temperature, and the properties and areas of nucleation substrates; (2) reactant (kaolin and, optionally, K-feldspar) and product (illite cement, illite replacement, and K-feldspar dissolution porosity) volumes; (3) the dimensions, volumes, and areas for the illite crystallite population; and (4) the K-Ar age for the authigenic illite with explicit consideration made for the effect of detrital contaminants.

### Illite Saturation State

The kinetics of crystal nucleation and growth both depend strongly upon saturation state (Lasaga, 1998). Variations in the saturation state of illite within reservoir sandstones are mainly determined by the activities of $SiO_{2(aq)}$, $Al^{+3}$, $K^+$, and $H^+$ (Bjørkum and Gjelsvik, 1988; Aagaard et al., 1992; Bjørlykke et al., 1995). In geologic settings where fibrous illite is actively forming, the activities of these species are likely to be controlled by mineral buffers present within the host sandstone (Hutcheon et al., 1993; Bazin et al., 1997a, b; Berger et al., 1997; Palandri and Reed, 2001). In formation waters above 100°C (212°F), $SiO_{2(aq)}$ concentrations tend to be at or near expected equilibrium values for quartz (Kharaka et al., 1985; Bjørlykke et al., 1995; Bazin et al., 1997a, b; Palandri and Reed, 2001). Kaolinite acts as an Al buffer and, like quartz, also buffers pH (Bazin et al., 1997a). Bazin et al. (1997b) argued that it is reasonable to assume that K-feldspar, when present, buffers $K^+$ activities in the absence of externally derived fluids.

We determined the likely saturation state of illite as a function of temperature in the presence of the quartz, kaolinite, and K-feldspar mineral buffers. The first step in this analysis is to calculate equilibrium activities for $SiO_{2(aq)}$, $Al^{+3}$, and $K^+$ as a function of temperature over the range of interest for illite formation in reservoir sandstones (we used Geochemist's Workbench™ version 6.0 for these calculations; Bethke, 1996). Although the silica activity for the buffered system increases with temperature, the opposite is true for dissolved aluminum (Figure 2A). Muscovite can be considered a thermodynamically stable proxy for illite. When the system is in equilibrium with quartz, the K-feldspar and kaolinite stability fields will be separated by the muscovite field over the full range of temperatures where illitization is likely to occur (Figure 2B) (Aagaard et al., 1992). Thus, there will be a thermodynamic drive for illite to form in the presence of K-feldspar and kaolinite in sandstone reservoirs. The next step in the analysis involves the determination of the equilibrium constant for muscovite with temperature (Figure 2C). The final step is to estimate the muscovite supersaturation state given its equilibrium constant and the activities of $SiO_{2(aq)}$, $Al^{+3}$, and $K^+$. Our calculations indicate that muscovite supersaturation in the presence of the mineral buffers increases systematically with temperature (Figure 2C). The magnitude of this increase is about a factor of 1.5 as temperature increases from 100 to 200°C (212 to 392°F).

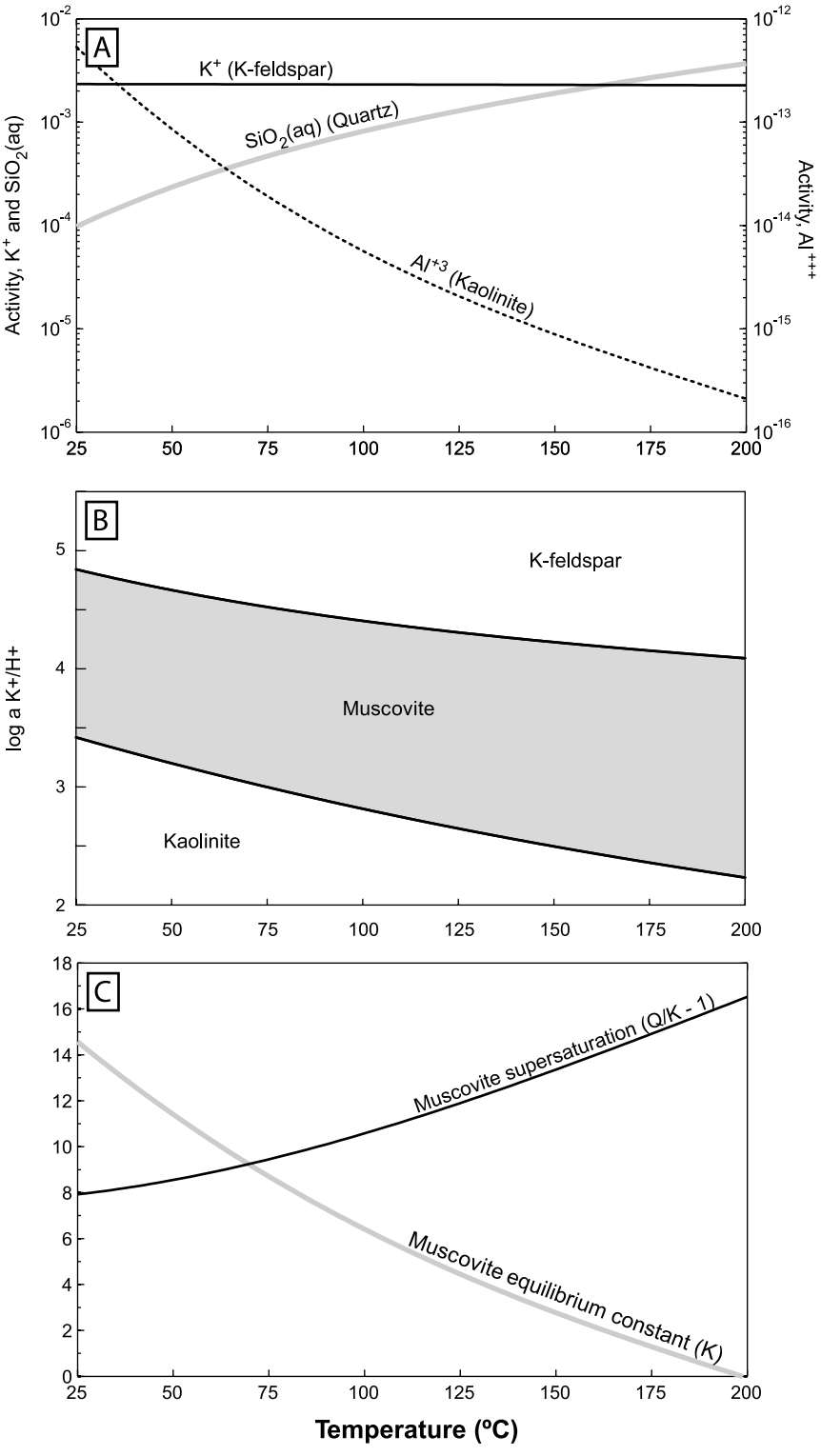


**Figure 2.** Calculated fluid compositions and extent of supersaturation for muscovite (a proxy for illite) as a function of temperature based on buffering by kaolinite, K-feldspar, and quartz. (A) Activities of $Al^{+3}$, $K^+$, and $SiO_2$(aq). (B) Stability fields for muscovite, kaolinite, and K-feldspar assuming equilibrium with quartz. (C) Muscovite equilibrium constant (K) and supersaturation state (Q/K-1).

Several workers suggest that illite formation in Rotliegende sandstones may have been influenced by externally derived evaporitic brines (Rossel, 1982; Macchi et al., 1990; Lanson et al., 1996). Brines with elevated $K^+$ activities could induce faster rates of illite formation by increasing illite supersaturation (Lanson et al., 1996). Consequently, we have formulated the model so that $K^+$ activities may be defined explicitly as an alternative to assuming control by a K-feldspar buffer. In such cases, the

model still considers that the quartz and kaolinite buffers control the $SiO_{2(aq)}$ and $Al^{+3}$ activities when determining the muscovite saturation state. The model also assumes in this case that K-feldspar, if present, is not a reactant. Thus, all Al in the fibrous illite is derived from kaolin and the system is fully open with respect to K.

## Crystal Nucleation

Wilkinson and Haszeldine (2002a) argued that nucleation is the primary control on the occurrence of fibrous illite cement in sandstones. Controls on crystallite nucleation, however, are the most poorly constrained aspect of kinetic models that could potentially be used to predict fibrous illite characteristics in sandstones because nucleation theory remains in the developmental stage and is difficult to test given that the nucleation process occurs at the atomic scale (Lasaga, 1998).

Illite fibers, like most diagenetic phases in sandstones, appear to form by heterogeneous nucleation, where nuclei adhere to the surfaces of preexisting solids because of the free energy benefits associated with the resulting lower surface area (Lasaga, 1998; Wilkinson and Haszeldine, 2002a). Experimentally grown illite fibers preferentially nucleate on muscovite substrates when they are present but eventually will form in the absence of such substrates (Chermak and Rimstidt, 1990). Little work has been done to date to rigorously document the nature of nucleation substrates for illite fibers in natural sandstones. However, documented examples of illite fibers nucleating on authigenic kaolin exist (Środoń and Eberl, 1984; Lanson et al., 1996, 2002) as well as quartz cement (Figure 1C) (Bonnell et al., 1999), and in some sandstones, illite pervasively covers all available pore-wall surfaces irrespective of composition (Lanson et al., 1996; Bjørlykke, 1998). Franks and Zwingmann (2010, this issue), in their study of illite in Permocarboniferous sandstones from Saudi Arabia, find that although illite fibers nucleate on detrital quartz grain and noneuhedral quartz cement surfaces, they do not occur on euhedral quartz faces. The scanning electron microscope (SEM) photomicrograph in Figure 1C, however, illustrates one instance where illite fibers appear to have nucleated on euhedral quartz faces. Thus, it appears that although illitic or micaceous material is the favored nucleation substrate for fibrous illite, such substrates are not an absolute requirement for nucleation. Furthermore, whereas there might be a tendency for illite fibers to avoid nucleating on euhedral quartz faces, it is not impossible for them to do so.

The critical nucleus size is an essential concept for illite nucleation models (Wilkinson and Haszeldine, 2002a). The critical nucleus represents a maximum in the Gibbs free-energy change over a spectrum in atomic cluster size that ranges from a few atoms to many millions of atoms in a crystal. The cluster size of the critical nucleus denotes the point where the increase in thermodynamic stability that comes with additions of atoms promotes continued crystal growth whereas removal of atoms increases the potential for nucleus dissolution. The abundance of critical nuclei is given by Lasaga (1998) as

$$N_{\mathrm{n}} = N_0 e^{\frac{-G_n}{RT}} \qquad (1)$$

where $N_0$ is the total number of moles in the medium (predominantly water), $G_n$ is the energy needed to form a critical nucleus consisting of $n$ molecular units, $T$ is temperature, and $R$ is the gas constant. By analogy with equation 1, we simulate the number of potential illite nuclei that form during a time interval $\Delta t$ (s) as

$$N = \left(A_{\mathrm{n}} e^{\frac{-\mathrm{Ea_n}}{RT}} \Delta t\right)\left(\frac{Q}{K} - 1\right) S_A \qquad (2)$$

where $A_{\mathrm{n}}$ is a pre-exponential probability factor (nucleation sites/cm$^2$/s), $\mathrm{Ea_n}$ is the activation energy for illite fiber nucleation (kJ/mol), $Q$ is the saturation state for muscovite, $K$ is the equilibrium concentration for muscovite, and $S_{\mathrm{A}}$ is the surface area available for nucleation. Increases in illite nuclei are thus expected with increasing supersaturation, temperature, and elapsed time. Increased nucleation rates could also result from lower activation energies for nucleation on substrates made

up of micaceous grains or detrital illitic clay compared to other surface types. Consequently, $Ea_n$ and $S_A$ may be defined independently for micaceous and nonmicaceous substrates in the model implementation.

We allow crystallites to nucleate on intergranular pore walls (Figure 1B, C) as well as on secondary pore walls associated with dissolution of K-feldspar grains (Figure 1D). The intergranular surface area is simulated through time by (Merino et al., 1983; Lichtner, 1988; Canals and Meunier, 1995; Lander et al., 2008)

$$S_{ig} = V_g\left(\frac{6}{D}\right)\left(\frac{\phi}{\phi_0}\right)^{2/3} \quad (3)$$

where $V_g$ is the grain volume in the model reference frame ($cm^3$), $D$ is the mean grain diameter (cm), $\phi_o$ is the intergranular porosity at the time of deposition (volume fraction), and $\phi$ is the current intergranular porosity (volume fraction). The fibrous illite model is integrated into Touchstone 7.0, which simulates the intergranular porosity through time based on the sandstone compaction state as well as the volume of illite and other cements. Touchstone also uses a proprietary algorithm to estimate the $\phi_o$ value based on mean grain size, sorting, and detrital matrix abundance. The nucleation area for moldic pores that form by K-feldspar grain dissolution is given by

$$S_{ksp} = \phi_{ksp}\left(\frac{6}{D}\right) \quad (4)$$

where $\phi_{ksp}$ is the volume of K-feldspar grains that have dissolved in the model reference frame ($cm^3$).

As discussed above, the formation of critical nuclei that could serve as the basis for new crystals requires a larger change in Gibbs free energy than is needed for an existing crystal to continue to grow. Therefore, in the near vicinity of a growing crystal, the degree of illite supersaturation will likely be somewhat lower compared to otherwise barren pore walls given that the crystal represents a sink for the dissolved reactants (Figure 3). This localized reduction in supersaturation would change the local free energy, making new nuclei less likely to form adjacent to growing crystals compared to crystal-free areas, and is analogous to what has been proposed for the control on nucleation of carbonate concretions at larger length scales (Walderhaug and Bjørkum, 1998). As new nuclei form and grow, the proportion of pore walls that are energetically favorable for creation of additional nuclei declines in the absence of changes in other factors (Figure 3). We consider this effect on nucleation by defining a characteristic radius of influence around each crystallite within which no new nuclei are allowed to form. The size of this area is likely to be a function of the diffusion rate (Kittel and Kroemer, 1980).

$$D_c = \frac{kT}{6\pi a\mu} \quad (5)$$

where $D_c$ is the diffusion coefficient, $k$ is the Boltzmann constant, $a$ is the size of particles in solution, and $\mu$ is the viscosity of the aqueous solution. In relatively dilute solutions, diffusion rates from equation 5 double from 100 to 160°C (212 to 320°F) thereby halving the expected radius of influence. Thus, we define the exclusion radius for nucleation of new crystallites in terms of the value at 100°C (212°F) and adjust the size using equation 5. Simulations can effectively neglect this potential effect on nucleation, if desired, by using a vanishingly small value for the radius of influence.

In a simulation, we define representative areas for nucleation on three types of surfaces: (1) intergranular pore walls that are made up of micaceous or illitic materials, (2) intergranular pore walls characterized by other materials, and (3) moldic pores after K-feldspar dissolution. We adjust the areas of these surfaces with each time step to account for changes in intergranular and secondary pore volumes. If illite reactants are present, we then determine the number of potential new nuclei for each area type and distribute them randomly over the currently available nucleation surface for that area. If a potential nucleus is located within the radius of influence of an existing crystal, however, it is not allowed to form.

An intriguing idea proposed by Wilkinson and Haszeldine (2002a) for fibrous illite, and discussed

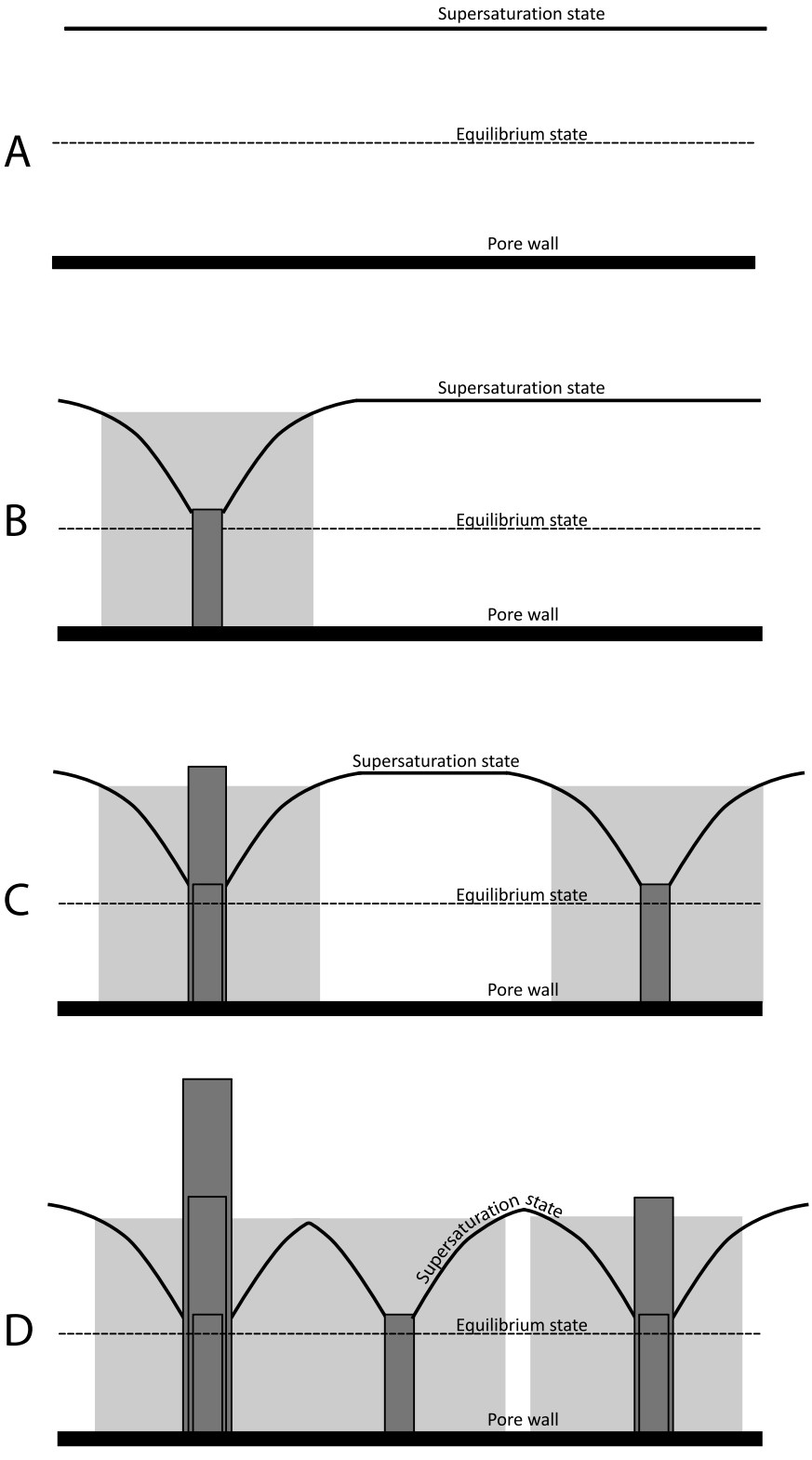


**Figure 3.** Schematic illustration of the potential influence of growing illite fibers on the nucleation of new crystallites. (A) Prior to crystallite nucleation, a given pore wall is likely to be exposed to fluid with a uniform degree in the extent of supersaturation for illite. (B) Once a crystallite nucleates, it acts as a sink for illite solutes thereby potentially reducing the extent of supersaturation in its immediate vicinity (gray region). (C) New crystals may be less likely to nucleate on the pore wall in the near vicinity of growing crystallites due to the lower local extent of illite supersaturation. (D) As additional crystallites form, the surface area that is amenable to the formation of new nuclei declines.

at greater length by Meunier (2006) for clay minerals in general, is that as crystallites become progressively larger, they eventually stop growing because of high strain energies that arise due to the cumulative influence of crystallographic defects. In such a scenario, it becomes energetically more favorable for a new crystal to nucleate and grow compared to continued growth on a large crystal.

Crystallite size distribution data for illite that formed in hydrothermal zones (Bove et al., 2002) and by smectite illitization (Środoń et al., 2000), however, show log-normal distributions that have been interpreted to result from faster surface-area normalized growth rates on larger crystallites compared to smaller counterparts (Eberl et al., 1998). This pattern of faster growth on larger crystals is the opposite of that expected from a scenario where increasing strain energy with size results in diminished potential for continued growth of larger crystallites. Regrettably no quantitative size distribution data are available to determine whether fibrous illite crystals in sandstone reservoirs also show log-normal size distributions. In light of these conflicting views and the lack of illite fiber data, we have elected not to incorporate any dependencies between crystallite size and the rates of nucleation or growth in our current model implementation.

## Crystal Growth, Reactant Dissolution, and Mass Balance

We assume in our model formulation that the rate of growth of fibrous illite crystals is slower than the potential rate of reactant dissolution and the potential rate of diffusion of dissolved reactants to illite growth sites. Consequently, the extent of reactant dissolution for a modeled time interval is determined by the volume of illite that grows in this precipitation rate limited system. These assumptions are consistent with the conclusions of Altaner (1986), who showed that K-feldspar dissolution rates are significantly faster than rates of smectite illitization.

We enforce the conservation of Al within the modeled frame of reference and permit illite to grow only when a source for both K and residual kaolin in the system exists. A simulation may be set to be either open or closed with respect to K. If the system is closed with respect to K, then K is exclusively derived from K-feldspar, which also provides an additional source of Al. For simulations that are defined as open with respect to K, we assume that in-situ K-feldspar dissolution does not contribute to illite formation and that kaolin therefore is the exclusive source of illite Al. Given that quartz cementation is ubiquitous in illite-bearing sandstones (at least when quartz nucleation area is available), we assume that there is never a shortfall in the supply of the Si needed for illite formation.

Güven (2001) showed that illite fibers are elongated along the crystallographic *a* axis. Although illite fibers tend to taper somewhat along the *a* axis (Lee, 1984; Nagy, 1994), we approximate the crystallite shape as a rectangular volume defined by length, thickness, and width. We assume that the crystallite proportions remain constant as they grow given that the growth surfaces for illite fibers are defined by euhedral crystal faces from early growth stages, and Nagy (1994) found a width to thickness ratio of around 17 for illite fibers over a range in particle sizes. Assessing the ratio of fiber length to width is more difficult. Dispersed particles as analyzed by transmission electron microscopy (TEM) and atomic force microscopy are likely broken during the sample preparation procedure and therefore only provide a minimum constraint. Data from these methods and SEM images of in-situ illite, however, suggest that a value on the order of 100 is reasonable.

We determine the extent of growth along the length of the crystal (*a* axis) over a time interval $\Delta t$ (s) as follows.

$$I_a = \left(\frac{m}{\rho}\right)\left(A_g e^{\frac{-Ea_g}{RT}}\Delta t\right)\left(\frac{Q}{K} - 1\right) \qquad (6)$$

where $I_a$ is the increase in fiber length (cm), $m$ is the molecular mass of illite (g/mol), ρ is the density of illite (g/cm$^3$), $A_g$ is a pre-exponential constant (mol/cm$^2$/s), $Ea_g$ is the activation energy for illite precipitation (kJ/mol), Q is the saturation state for muscovite, and $K$ is the equilibrium constant for muscovite. After determining the extent to which a crystal lengthens, we modify its thickness and width proportionally. The thicknesses of the crystallites, however, are restricted to integral values of 0.001 $\mu$m given that this represents one unit cell for illite along the crystallographic $c^*$ direction. The crystallite volume ($V_c$) is determined as

$$V_c = L_c W_c T_c \qquad (7)$$

where $L_c$ is the crystal length along the *a* axis, $W_c$ is the crystal width perpendicular to the *a* axis, and $T_c$ is the crystallite thickness along the $c^*$ axis. As the crystal grows, the model keeps track of excess thickness and adds a new illite unit cell to $T_c$ once the excess reaches 0.001 $\mu$m. By excluding this excess thickness in the volume calculation, we obtain a more accurate illite K mass determination for simulation of K-Ar ages. We calculate the crystallite wetted surface area ($A_c$) by assuming that the entire surface of the crystallite is in contact with the pore fluid except for where it is attached to the pore wall.

$$A_c = 2(L_c W_c) + 2(L_c T_c) + T_c W_c \qquad (8)$$

The model tracks the dimensions, volume, and surface area for each simulated crystallite in addition to the nucleation time and the time at which it ceased to have the potential to grow due to local porosity occlusion. A crystal is not permitted to continue to grow, even if reactants are available, when it is located in the part of the simulated nucleation area that has been removed due to porosity loss that arises from cementation or continued compaction. In accordance with Nagy's (1994) observations, we assume that no Ostwald ripening occurs for the crystallite population. Thus, once formed, a simulated illite fiber never dissolves. This assumption appears to be reasonable over the temperature range experienced by many hydrocarbon reservoirs. At temperatures in excess of approximately 150°C (302°F), however, this assumption may not be valid because fibrous illite may begin to dissolve while more equant crystallites form (Lanson et al., 2002) such that eventually the $2M_1$ polytype predominates over the 1M polytype characteristic of fibrous illite (Hunziker, 1986; Jahren and Aagaard, 1989).

## Illite K-Ar Ages

Much literature is concerned with the use of illite K-Ar ages for inferring the timing and likely driving forces for illite formation. Thus, K-Ar ages provide an important potential means to test and calibrate the fibrous illite model. Consequently, the model determines K-Ar ages by considering the volume fraction of illite that formed through the burial history of the sample. The K-Ar calculations are made using the decay constants of Steiger and Jäger (1977).

Although the illite K-Ar systematics are well understood (Lee, 1984; Lee et al., 1985, 1989; Hamilton et al., 1989, 1992; Clauer and Chaudhuri, 1995), the interpretation of the meaning of illite K-Ar ages is not so straightforward (e.g., Ehrenberg and Nadeau, 1989; Clauer et al., 1992; Matthews et al., 1994; Bjørlykke, 1998; Zwingmann et al., 1998; Pevear, 1999; Ylagan et al., 2000; Środoń et al., 2002; Wilkinson and Haszeldine, 2002b; Meunier et al., 2004; Szczerba and Środoń, 2009). Two common assumptions in the analysis of illite fiber K-Ar ages are that (1) illite in the finest size fraction represents the last formed illite and (2) the K-Ar age of this illite represents the time of cessation of illite growth (Lee, 1984; Hamilton et al., 1989). Two potential problems with these assumptions exist. First, even if this fraction of the illite was the last to form, this does not necessarily mean that the growth duration was geologically instantaneous. Thus, in the absence of contaminants, the date reflects the volume-weighted average of when the analyzed illite fibers grew (Hamilton et al., 1989). Second, the extent to which the smallest illite fraction actually represents the last formed illite is unclear. Little is known about how the sample preparation procedure impacts the in-situ particle size distribution or if early formed small crystallites that stopped growing due to interference with other solids (including other illite fibers) may also be found within the smallest size fraction.

Even the smallest size separates used for K-Ar analysis are likely to contain some extent of detrital contamination. This contamination in some cases may lead to K-Ar ages that are significantly older than what would be derived from pure authigenic illite, particularly for sandstones that contain detrital clay matrix or grains rich in K-feldspar, mica, or detrital illite (e.g., Hamilton et al., 1989, 1992; Glasmann, 1992; Zwingmann et al., 1998, 1999; Girard et al., 2002). Consequently, we also determine an additional K-Ar age that incorporates the ages and volume abundances of the following

**Table 1.** Stoichiometry, Density, and Microporosity Values Used for Mass-Balance and K-Ar Calculations*

| Mineral | Stoichiometry | Density (g/cm$^3$) | Microporosity (vol.%) |
|---|---|---|---|
| Illite | $K_{0.91}Al_{2.21}Fe_{0.04}Mg_{0.15}Si_{3.51}O_{10}(OH)_2$ | 2.75 | 65 |
| Kaolinite | $Al_2Si_2O_5(OH)_4$ | 2.60 | 50 |
| K-feldspar | $KAlSi_3O_8$ | 2.56 | 0 |
| Plagioclase feldspar | $K_{0.05}Na_{0.60}Ca_{0.35}Al_{1.35}Si_{2.65}O_8$ | 2.67 | 0 |
| Muscovite | $KAl_3Si_3O_{10}(OH)_2$ | 2.82 | 0 |

*Illite stoichiometry is from Lander et al. (1990) and mineral densities are from Deer et al. (1966).

contaminant phases: K-feldspar, muscovite, and detrital illite.

In light of this discussion, we determine several different age values in the simulations for comparison with K-Ar measurements: (1) the K-Ar age for all authigenic illite fibers integrated over the complete illitization history, (2) the K-Ar age with detrital contaminants, (3) the times when the 10th, 50th, and 90th volume percentiles of authigenic illite form, (4) the time of the peak rate for illite growth, and (5) the time of the cessation of illite formation in association with the exhaustion of reactants or the occlusion of pore space needed for continued growth.

## Reconstructing Reactants

We have designed the model so that it may be used to simulate the geologic progression of the reaction for already illitized samples. The model reconstructs K-feldspar for the case where it is considered to be the illite K source as well as the amount of kaolin that reacted to form illite. The parent materials for kaolinite also are reconstructed by Al mass balance. These mass-balance calculations account for the stoichiometries and densities of the associated minerals in addition to microporosity values for the authigenic kaolinite and illite (see Table 1 for the values used for simulations in this article).

For simulations that assume that the illite K is derived from K-feldspar, the starting point is to reconstruct the depositional composition by determining the amount of K-feldspar dissolution needed to account for the K bound in illite. This value is then compared to the amount of K-feldspar dissolution indicated by secondary porosity from K-feldspar dissolution together with K-feldspar replacement by illitic phases. Even if K actually is conserved within the sample frame of reference, it is unlikely that these two measures of the volume of dissolved K-feldspar will be in precise agreement given the uncertainties in the petrographic data, microporosity values, and illite stoichiometry used for the analysis. Thus, the amount of K-feldspar to add to the depositional composition may be based either on the illite derived value or on the value determined from K-feldspar secondary porosity and illite replacement.

The next step in the reconstruction is to conduct an Al mass analysis. Here, we determine the Al associated with measured kaolinite and illite abundances in light of their microporosities, stoichiometries, and densities. If K-feldspar is considered to be the illite K source, then we subtract the illite Al that is derived from K-feldspar dissolution from the total Al bound in illite. We then assume that the remaining illite Al is derived from kaolinite dissolution. We add to this value the Al associated with any measured kaolin in the sample to determine the total Al produced by dissolution of plagioclase feldspar, muscovite, biotite, or additional K-feldspar. We compare this Al mass to the petrographically determined extent of dissolution and replacement of these additional potential Al sources. As with the K mass balance, we do not expect a precise agreement between the Al mass based on the petrographic evidence for grain dissolution and replacement and the Al mass based on the authigenic clays. Consequently, we have designed the model so either of these two calculation methods may be used for the Al reconstruction.

The reconstruction process adds feldspar and mica to sample-measured values to derive the depositional abundances of these minerals. We then use paragenetic rules (defined in terms of burial depth, temperature, or absolute geologic time constraints) to determine when these minerals react to form kaolinite. Illite may then form according to the model characteristics and input data described above.

## MODEL BEHAVIOR

Although the veracity of any geological model is best determined by testing its predictions using natural data sets, synthetic simulations of simplified geologic scenarios are useful for understanding the model behavior. Thus, as a prelude to our evaluation of the model performance, we use synthetic simulations as a means to explore model sensitivity to nucleation and growth kinetics, temperature history, reactant volumes, $K^+$ activities, and the nature of nucleation substrates.

### Approach for Constraining Kinetics

Perhaps the greatest controversy in the application of chemical kinetic models for simulation of diagenetic processes has to do with the appropriate approach for determining rate constants. Although laboratory studies provide a critical understanding of the controls on kinetic rates, growing evidence shows that the associated rates may be much faster than those found in geologic environments, at least for silicate phases. The dichotomy between natural and laboratory-derived rate constants has been well documented, for example, for feldspar dissolution (e.g., Blum and Stillings, 1995; White and Brantley, 2003; Zhu, 2005; Maher et al., 2006) and quartz precipitation (e.g., Walderhaug, 1994, 1996, 2000; Oelkers et al., 2000; Worden and Morad, 2000; Lander et al., 2008) where laboratory rates may be as much as five orders of magnitude greater than rates derived from geologic observations. Several studies have attempted to apply laboratory-derived rate constants for fibrous illite growth (e.g., Chermak and Rimstidt, 1990) to geologic settings. These rate constants lead to rapid, pervasive illitization at much lower temperatures than are observed in nature. For example, Brosse et al. (2000) found that laboratory-derived rates suggest that pervasive illitization would occur in about 20,000 yr at 105°C (221°F) in North Sea reservoirs but point out that parts of the reservoir that are at present-day temperatures of 110°C (230°F) contain only trace amounts of illite while having abundant K-feldspar and kaolinite reactants. Likewise, Berger et al. (1997) found that laboratory kinetics predict pervasive illitization to occur in typical formation waters within 4.5 m.y. at 50°C (122°F) and in a mere 15,000 yr at 80°C (176°F), despite ample field evidence showing the coexistence of kaolinite and K-feldspar reactants over millions of years at these and higher temperatures (Berger et al., 1997). However, Nagy (1994) and D. N. Awwiller (unpublished presentation to the SEPM Clastic Diagenesis Research Group in 1998) suggested that changes in particle dimensions with depth imply illite fiber growth rates that are similar to the much slower rates of quartz cement growth that are implied by empirical calibration to geologic data.

Our view is that a model that aims to predict the occurrence and properties of illite in reservoir sandstones should incorporate kinetic parameters that are based on empirical calibration to geologic observations instead of laboratory rates that are in apparent conflict with these observations. Thus, in the following analysis, we use kinetic parameters that lead to pervasive illitization over time and temperature ranges that are consistent with geological constraints on illite occurrence.

### Baseline Case

We begin our sensitivity analysis by considering suites of kinetic parameters that lead to illitization patterns that are broadly consistent with data from Norwegian Shelf reservoirs of Jurassic age. In these sandstones, incipient illite formation is observed at present-day temperatures near 120°C (248°F), and pervasive illitization is characteristic of reservoirs with present-day temperatures of 140°C (284°F) (e.g., Bjørlykke et al., 1986; Ehrenberg and Nadeau,

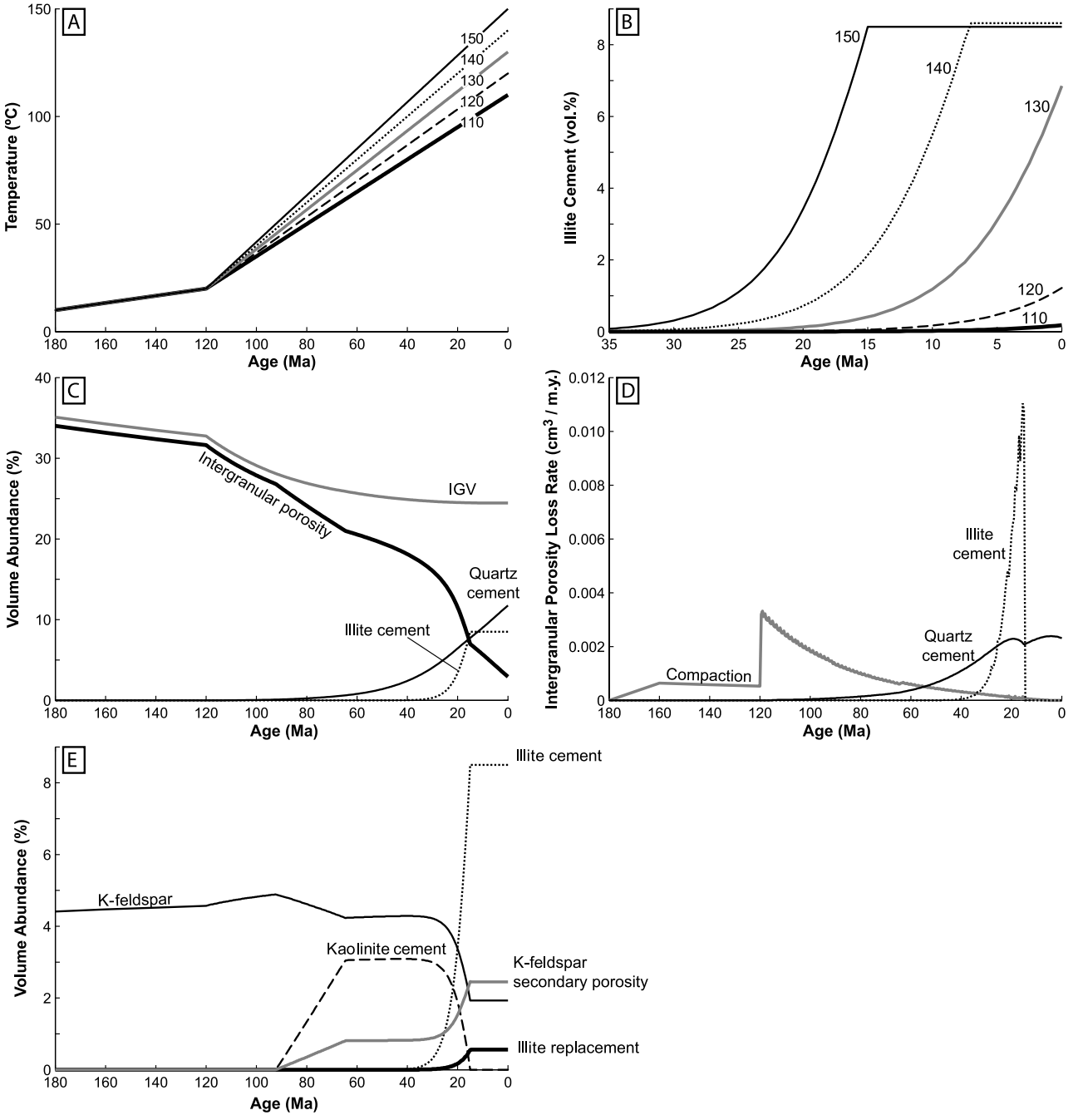


**Figure 4.** Input and results for the baseline set of synthetic illitization models that are designed to roughly approximate illite formation in Jurassic reservoirs in the North Sea and Norwegian Shelf. (A) Temperature history input. (B) Simulated illite cement abundance with geologic time for each of the temperature histories. (C) Modeled change in intergranular volume (IGV, a proxy for compaction state), intergranular porosity, quartz cement, and illite cement with geologic time for the maximum 150°C simulation. (D) Comparison of modeled rates of the pore volume loss due to compaction, quartz cementation, and illite cementation with geologic time for the maximum 150°C simulation. (E) Evolution in the volume abundance of illite reactants and products with time for the maximum 150°C burial history.

1989; Glasmann et al., 1989; Ramm and Ryseth, 1996; Chuhan et al., 2001). The simulations incorporate a series of temperature histories with a common depositional time of 180 m.y. but with maximum temperatures that range from 110 to 150°C (230 to 302°F) (Figure 4A). For model

input, we use a well-sorted, upper medium-grained sandstone with a subarkosic composition that is based on the characteristics of petrographically analyzed samples from the Garn Formation. The present-day sandstone composition has 3.2 and 1.2 vol.% of K-feldspar and plagioclase feldspar, respectively. In addition, we assume that 3 vol.% of kaolinite formed early in the burial history from the dissolution of equal volumes of plagioclase feldspar and K-feldspar. The simulations account for the effect of compaction and quartz cementation on the porosity and nucleation surface area by the coupling of the illite model with Touchstone 7.0 models for these processes (Lander et al., 2008).

The kinetic parameters we use not only lead to pervasive illitization (all available reactants are consumed) by 140°C (284°F), but are also in agreement with the data for these reservoirs that indicate that samples with maximum temperatures of 120°C (248°F) have experienced only incipient illite formation (Figure 4B). The value for the activation energy for illite precipitation ($Ea_g$) of 73 kJ/mol is substantially higher than the 60.7 kJ/mol value we used for quartz cementation, which is based on empirical calibration to a Jurassic data set from the Norwegian Shelf (Lander et al., 2008) (we used an $A_g$ value of $-9 \times 10^{-12}$ mol/cm$^2$/s for both the illite and quartz models). For the nucleation parameters, we used values of 8000 sites/cm$^2$/m.y. for $A_n$ and 73 kJ/mol for $Ea_n$. We also assumed that no new illite nuclei would form within 0.002 $\mu$m of an existing crystallite at a reference temperature of 100°C (212°F) (we adjusted this range with temperature using equation 5).

In the simulation using a burial history with a maximum temperature of 150°C (302°F), illite formation begins much later than compaction or even quartz cementation (Figure 4C). Once illitization begins in earnest, however, it reduces intergranular porosity at rates that greatly exceed loss rates associated with compaction or quartz cementation (Figure 4D). Although illitization becomes significant much later than quartz cementation, the simulation shows that quartz cementation is likely to continue after the illitization process is complete provided that adequate nucleation surface area remains (Figure 4C). This result is consistent with observations that indicate that although illite fibers nucleated and grew on quartz overgrowths in Norwegian Shelf reservoirs, they were engulfed by subsequent quartz cement growth (Bonnell et al., 1999).

The fate of the reactants and products involved in the illitization reaction is shown with time for the maximum 150°C simulation in Figure 4E. We set up the simulation so that kaolinite formed in association with K-feldspar and plagioclase (not shown) dissolution over a temperature range of 50 to 80°C (122 to 176°F). The coexisting kaolinite and residual K-feldspar remained relatively unaffected until about 28 Ma when the sandstone reached 120°C (248°F). From this time onward, these phases dissolved and illite began to form. Although the dissolution of K-feldspar produced additional secondary porosity, this porosity was partly occluded by illite that grew within these pores, creating a replacement texture. Likewise, the intergranular porosity increase associated with kaolinite cement dissolution was more than compensated for by intergranular porosity loss from both illite and quartz cements (Figure 4C). The reaction ceased when all kaolinite was consumed leading, in this scenario, to residual K-feldspar.

In addition to matching the illitization pattern with present-day temperature, the nucleation kinetic parameters also lead to predicted fiber thicknesses that are consistent with data from North Sea reservoirs. Average particle thicknesses for illite-size separates obtained by Nagy (1994) tend to thicken with the present-day reservoir temperature (Figure 5). The data shown in Figure 5 are average values derived from measurements made on illite fibers in two size separates: less than 0.02-$\mu$m equivalent spherical diameter and 0.02- to 0.2-$\mu$m equivalent spherical diameter. We have overlain on this figure the simulated present-day 10th, 50th, and 90th percentile (P10, P50, and P90) crystallite thicknesses (by crystallite count) for the simulations. These simulated ranges span the measurements and also show an increase with temperature. Although the P50 and P90 sizes show a larger increase with temperature than the measurements, such a discrepancy seems logical given

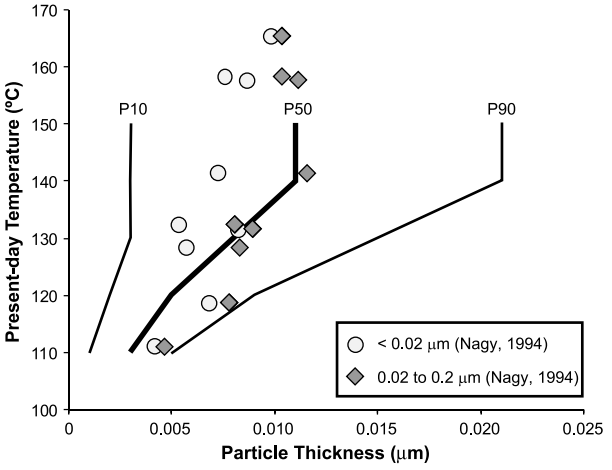


**Figure 5.** Comparison of the average values for measured illite fiber thicknesses for North Sea reservoirs (Nagy, 1994) with simulated values for the baseline case set of synthetic models. The simulated values are shown as the 10th, 50th, and 90th percentile values (P10, P50, and P90, respectively) for the particle size distribution where the percentiles are based on the number of simulated illite fibers.

that the size separation procedure, by design, is biased toward the finer part of the crystallite size distribution.

## Sensitivity to Kinetic Parameters

We evaluated the sensitivity of model results to the activation energies for illite nucleation and growth using the 150°C maximum burial history (Figure 4A) and the baseline sandstone composition and texture. For these simulations, we adjusted the kinetic parameters such that the peak rate of illitization occurs at 140°C (284°F) for all scenarios. Results show that slower crystal growth rates (larger $Ea_g$ values) must be counterbalanced by faster nucleation rates (smaller $Ea_n$ values) to maintain this peak illitization temperature (Figure 6A). Stated in another way, if the crystal growth rate slows, then growth must occur on more crystals to maintain a fast net precipitation rate. Consequently, when the crystal growth rate decreases in these runs, the simulated crystal sizes (as exemplified by the P50 thicknesses) decline systematically (Figure 6B). The simulations also show a systematic increase in the duration of illitization (as indicated by the elapsed time between the precipitation of the 10th and 90th volume percentiles) as the crystal growth rate decreases (Figure 6B).

## Sensitivity to Temperature History

We evaluated the model sensitivity to thermal exposure by maintaining the same temperature

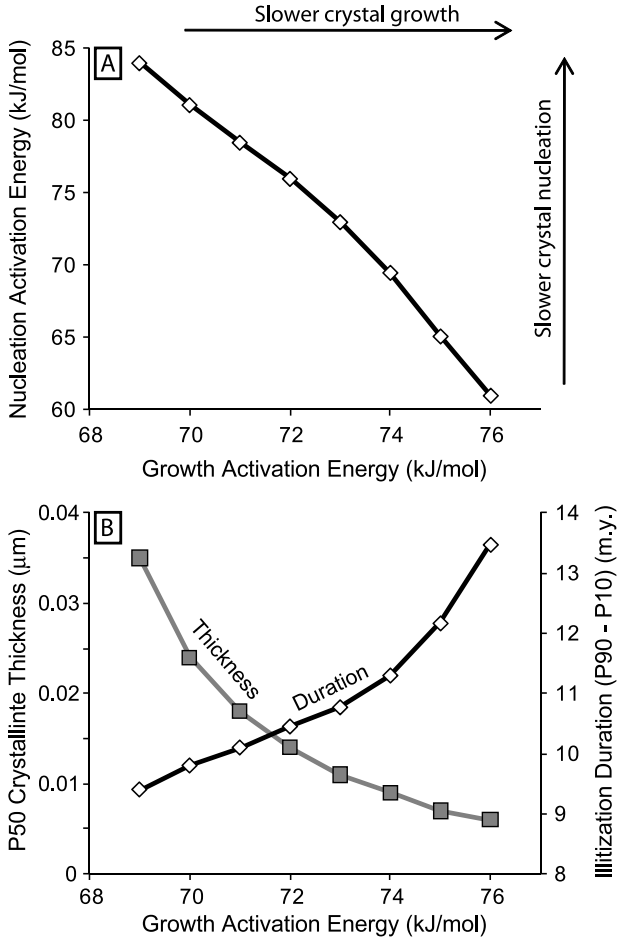


**Figure 6.** Sensitivity of simulation results to the activation energies for illite nucleation ($Ea_n$) and growth ($Ea_g$) where all model scenarios are constrained to lead to a peak rate of illitization at 140°C (284°F) for the maximum 150°C temperature history (Figure 4A) and baseline sandstone composition and texture. (A) Slower crystal growth from larger growth activation energies must be counterbalanced by faster crystal nucleation (lower nucleation activation energy) to maintain the same peak temperature for illite formation. (B) The P50 crystal thicknesses decrease systematically as growth rate decreases ($Ea_g$ increases) and nucleation rate increases. Faster crystal growth rates also result in faster overall rates of reaction as exemplified by the time duration between when the 10th and 90th volume percentiles (P10 and P90, respectively) of the present-day illite volume formed.

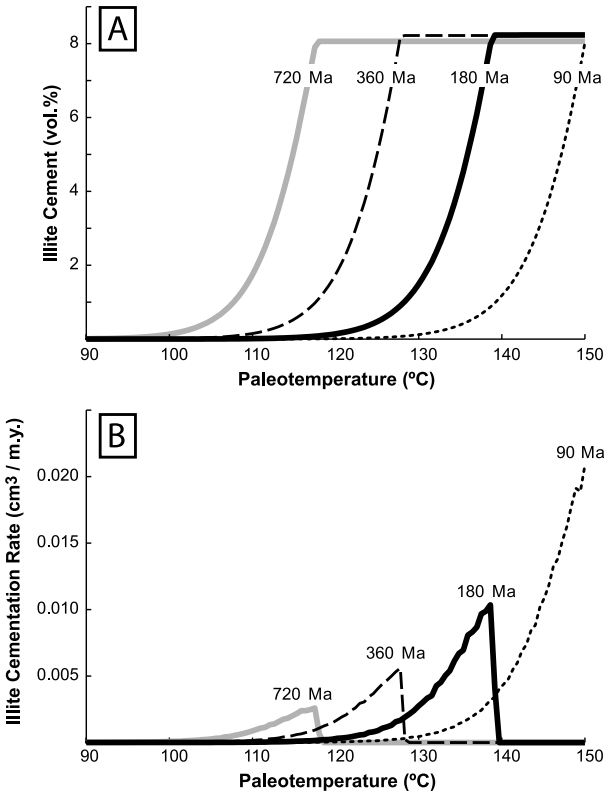


**Figure 7.** Sensitivity to thermal exposure for scenarios where the same temperature values are used as the maximum 150°C baseline scenario (Figure 4A) but the time durations change. (A) The temperature of pervasive illitization increases roughly by 10°C (18°F) when the time duration is halved. (B) The rates of illitization increase progressively with decreasing time duration for those scenarios with pervasive illitization.

history values used for the 150°C maximum scenario for the baseline case (Figure 4A) while scaling the time duration such that the time of deposition ranged from 720 to 90 Ma. We used the same kinetic parameters and sandstone composition and texture as used for the baseline case. The simulated temperature of pervasive illitization drops by roughly 10°C (18°F) for each doubling of the burial history time duration (Figure 7A). The simulations also show progressively greater peak illitization rates as the time duration decreases (Figure 7B). This pattern occurs because the shorter residence time within a given temperature range for the younger burial histories means that less reactant is consumed before progressing to the higher temperatures associated with the next burial history step. Consequently, greater volumes of reactants persist to higher temperatures where illite nucleation and growth rates are faster.

## Sensitivity to Reactant Volumes

In this set of sensitivity runs, we varied the amounts of kaolinite and K-feldspar reactants while keeping all other factors the same as the baseline case with the maximum 150°C burial history scenario (Figure 4A). Results show that although the rate of illitization is equivalent for each simulation while reactants are available, the reaction is able to continue to higher temperatures for simulations with greater reactant volumes (Figure 8). Thus, in the absence of other differences, results indicate that sandstones with greater reactant volume should have younger integrated ages of illite formation while having higher peak illitization rates at hotter temperatures (Figure 8).

## Sensitivity to $K^+$ Activity

Increasing $K^+$ activity leads to faster rates of both crystal nucleation and growth because it causes a higher degree of supersaturation for the muscovite proxy to illite. We used the maximum 150°C burial history scenario from the baseline case (Figure 4A) together with log $K^+$ activities of –3, –2, and –1 to assess the impact of this factor on the simulated timing of illitization with respect to a case where $K^+$

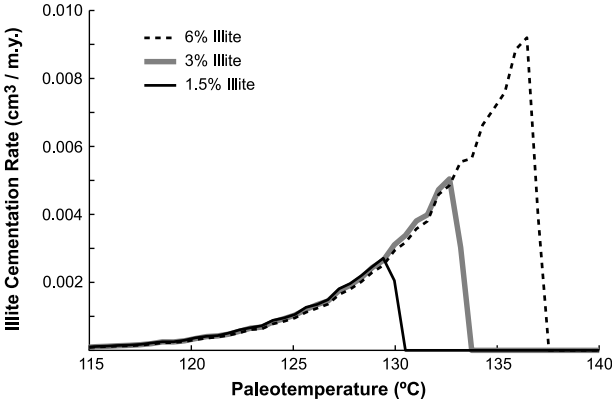


**Figure 8.** Sensitivity to reactant volumes for scenarios where other compositional and textural characteristics are constant using the baseline maximum 150°C burial history (Figure 4A). The illite cementation rates are independent of reactant volumes so long as reactants are available. For samples with greater reactant volumes (greater final illite abundances), the reaction takes longer to complete, occurs at higher temperatures, and reaches faster peak rates.

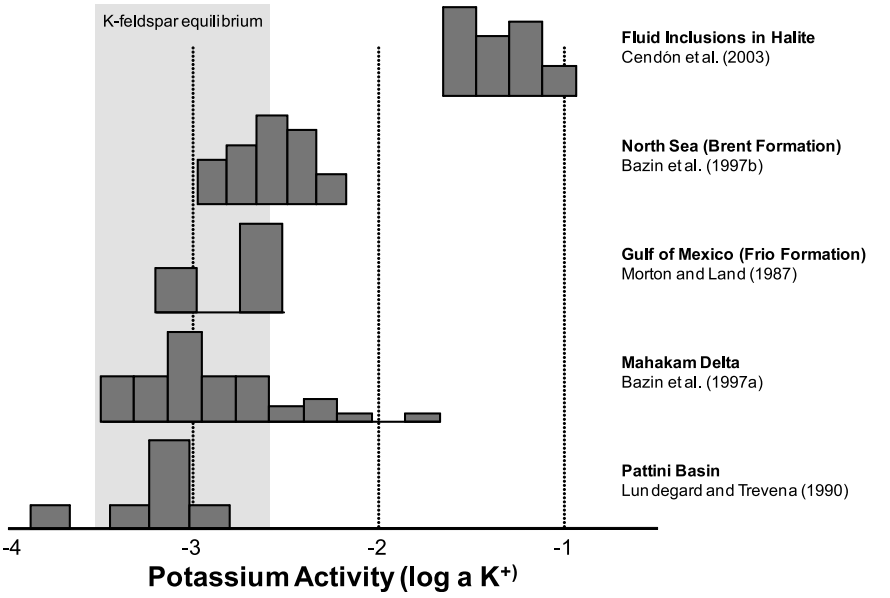


**Figure 9.** Calculated $K^+$ activities from published fluid compositional analyses collected from sandstone reservoirs and from fluid inclusions in halite. We calculated the activities with Geochemist's Workbench™ 6.0 (Bethke, 1996) using the Debye-Hückel method except for the fluid derived from halite inclusions where we used the Pitzer method. The shaded region indicates the range in $K^+$ activities expected for equilibrium with K feldspar.

activity is controlled by equilibrium with K-feldspar. The –2 log $K^+$ activity scenario is at the upper end of the range shown by formation waters reported for several Mesozoic and Tertiary reservoirs, whereas the –1 value corresponds to the upper end of values determined from fluid inclusions in halite crystals (Figure 9). The simulations also assume that the system is open with respect to $K^+$ and that K-feldspar is not a reactant.

Simulation results, as expected, are profoundly influenced by increasing $K^+$ activity. Illitization is complete by 95°C (194°F) for the log a $K^+$ –2 scenario compared to 138°C (275°F) for the K-feldspar equilibrium baseline case (Figure 10A). At temperatures above 60°C (140°F) in the log a $K^+$ –1 scenario, kaolinite is consumed more rapidly than it forms (Figure 10B). Thus, the time of the reaction completion for this geologically unrealistic scenario is determined by the constraints used to define the formation of the kaolinite reactant. The overall abundance of illite that forms is lower for these high $K^+$ activity scenarios compared to the baseline case because K-feldspar does not contribute Al for illite growth (Figure 10A).

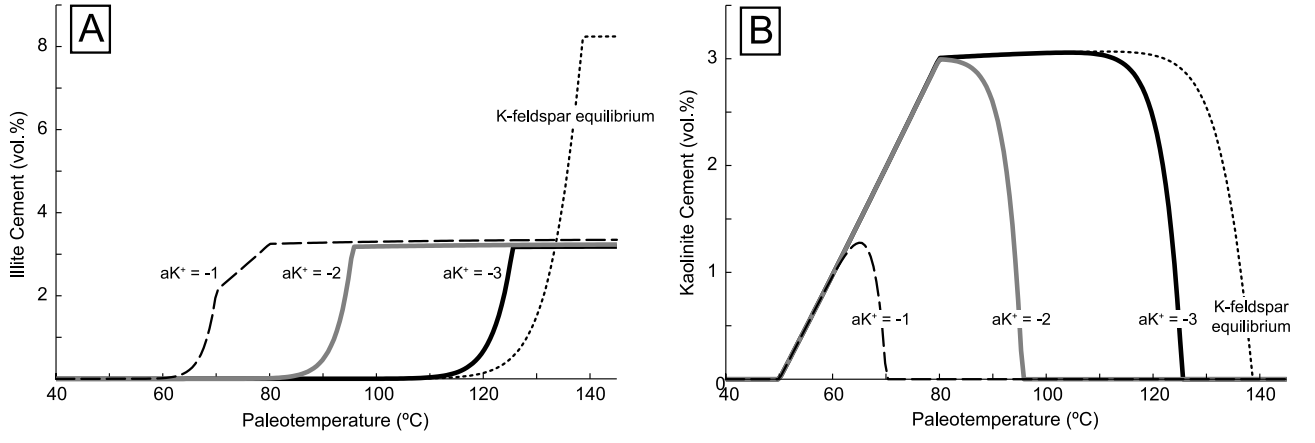


**Figure 10.** Sensitivity to $K^+$ activity using the baseline composition and texture and the maximum 150°C temperature history (Figure 4A). (A) Simulated illite cement with paleotemperature. The temperature of illitization drops greatly with increasing $K^+$ activity. The final illite abundance is greater for the K-feldspar equilibrium run because the feldspar provides an additional source for illite Al. (B) Simulated kaolinite cement with paleotemperature. Although the same volume of kaolinite forms in all runs, in the scenario with a log $K^+$ activity of –1, the rate of the reaction is sufficiently fast enough that it is consumed faster than it forms at temperatures greater than 70°C (158°F).

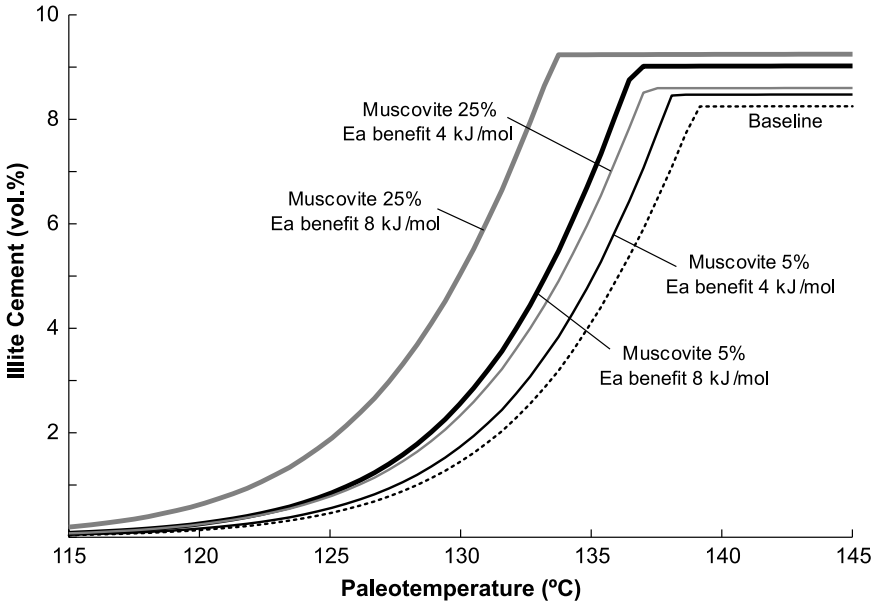


**Figure 11.** Sensitivity of illite cement abundance to preferential nucleation on muscovite grains using the baseline texture and the maximum 150°C temperature history (Figure 4A). Preferential nucleation on muscovite leads to a lower temperature for the completion of the illitization reaction and a greater fraction of the illite occurrence as cement (in intergranular pores) compared to "replacement" (in grain dissolution pores). The magnitude of the effect, however, is minor for the two scenarios with 5-vol.% muscovite. In the maximum effect case (25-vol.% muscovite and an activation energy for nucleation on muscovite that is 8 kJ/mol lower than on other substrates), the temperature for completion of the reaction is about 5°C (9°F) cooler than the baseline.

## Sensitivity to Nucleation Substrate Properties

The model is designed to consider preferential nucleation of fibrous illite on substrates such as micaceous or illitic surfaces by providing a means to specify the activation energy benefit for nucleation on such substrates compared to other surface types and by accounting for the fraction of the intergranular pore area that is made up of such substrates. To illustrate the model sensitivity to these two factors, we defined muscovite grains to be a preferential nucleation substrate. We considered scenarios where we decreased the activation energy for nucleation by 4 and 8 kJ/mol for muscovite surfaces compared to other substrate types for simulated samples with 5 and 25 vol.% of muscovite grains. Other factors in the simulations are as defined for the baseline case with the maximum 150°C burial history (Figure 4A).

Results indicate that preferential nucleation on micaceous substrates leads to pervasive illitization at lower paleotemperatures (earlier in the burial histories) compared to the baseline case (Figure 11), although the crystal growth kinetics are held constant. The faster overall illitization occurs in the preferential nucleation scenarios because growth occurs on a larger number of crystals. Additionally, preferential nucleation substrates promote illite formation as cement compared to replacement (where the crystals grow within secondary pores after K-feldspar dissolution). This preference for cement occurs because the preferential nucleation substrates border intergranular pores. The significance of preferential nucleation on illite texture and timing, however, is comparatively minor except when the surface area made up of preferential substrates is a significant fraction of the overall area, and the activation energy benefit for nucleating on such surfaces is very large.

## Summary of Sensitivity Test Results

The sensitivity analysis reveals several noteworthy characteristics of the fibrous illite model. (1) Otherwise comparable sandstones with similar maximum temperatures but longer thermal residence times will tend to become pervasively illitized at lower temperatures and at slower overall rates. (2) Incursion of potassic brines into kaolinite-bearing sandstones leads to dramatic decreases in the temperatures of pervasive illitization compared to scenarios where K is derived from in-situ dissolution of K-feldspar. (3) Illitization takes longer to complete in sandstones with more reactants. (4) The presence of illitic or micaceous substrates that could act as preferential nuclei for illite crystals is unlikely to significantly affect the timing of illite formation except for sandstones that are highly micaceous, that have abundant illite-rich or muscovite-rich rock fragments, or that have grains

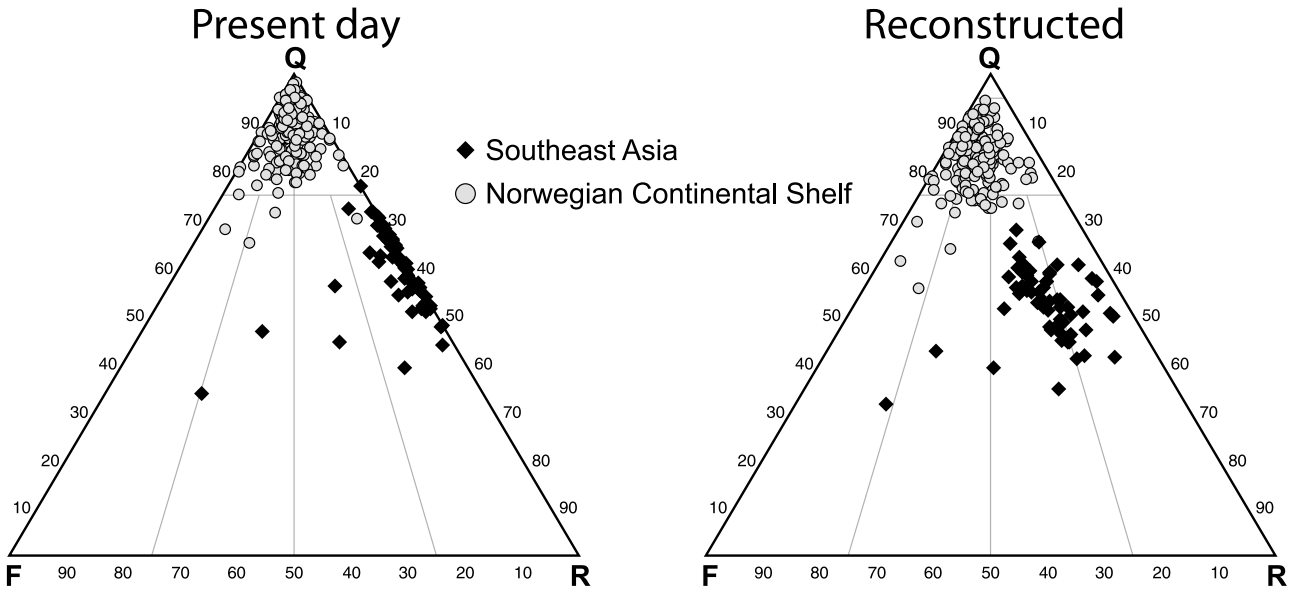


**Figure 12.** Quartz, feldspar, and rock fragment (QFR) ternary diagrams showing sample data for the two analyzed data sets using the classification scheme of Folk (1980). (A) Plot based on petrographic data. (B) Plot of reconstructed compositions for the time of deposition. The additional reconstructed rock fragment and feldspar values are based on (1) the interpretation of parent grains for petrographically determined grain dissolution and replacement and (2) the additional feldspar dissolution, if required, to account for Al and K in kaolin and illite assuming mass balance on the thin-section scale.

with well-developed detrital or infiltrated illitic coatings.

## APPLICATION TO GEOLOGIC DATA SETS

Although the synthetic simulations are useful for demonstrating model behavior, the model utility can only be determined by assessing the degree to which it reproduces geologic observations. We evaluated the performance of the model on two illite-bearing data sets: Jurassic sandstones from the Norwegian Continental Shelf (NCS) and Miocene sandstones in offshore Southeast Asia (SEA). In these data sets, the reaction of kaolin and K-feldspar appears to be the main source for authigenic illite given that both reactants are present, some illite appears to have inherited the morphology of kaolin that it replaced, and most authigenic illite has a fibrous habit (as opposed to a morphology more consistent with replacement of a smectitic precursor phase). Samples in both data sets have mean grain sizes ranging from very fine to very coarse and have sorting ranging from well to poor. The SEA samples are dominantly fluvial in origin, whereas the NCS samples are mainly shallow-marine sandstones with some tidal influences. The NCS data set is composed of 189 samples from 12 wells, and the SEA data set is made up of 62 samples from three wells. Sample framework-grain compositions are shown in Figure 12, and the range in sample temperature histories is shown in Figure 13.

Our objective for this work is to determine whether model results are consistent with the observed patterns of occurrence and abundances of illite, kaolinite (or dickite for higher temperature samples), and K-feldspar in the two data sets. Additionally, we compare predicted illite K-Ar results with available data and simulated fiber thicknesses with measurements from North Sea sandstones. The simulations we describe below use the mass-balance option that ensures that each simulated sample has sufficient reactants to account for the measured volumes of authigenic kaolin and illite. Thus, additional feldspar reactants are added at the time of deposition to maintain mass balance if the Al or K in the illite and kaolinite exceeds the amount associated with feldspar secondary porosity and replacement. Although this model configuration ensures sufficient reactants to account

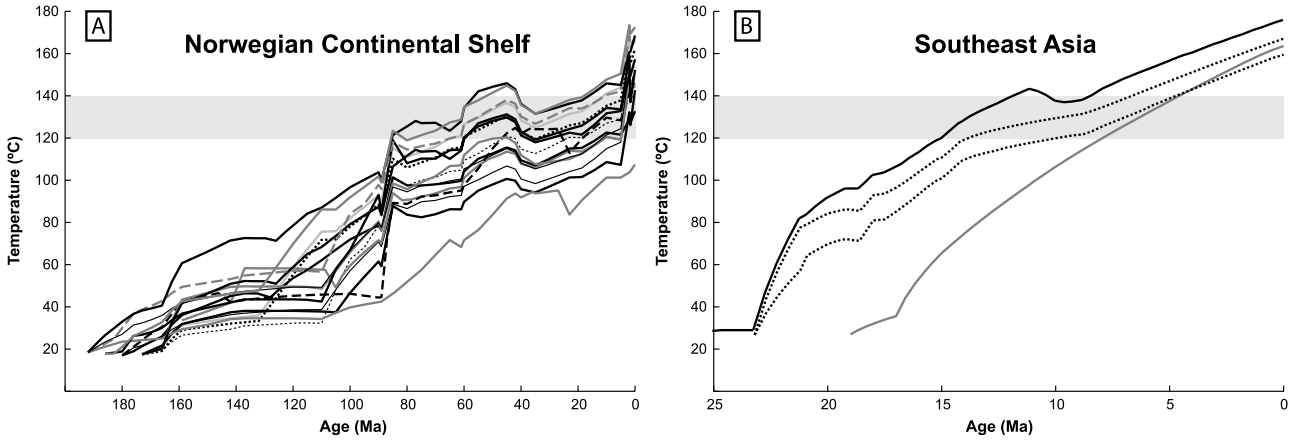


**Figure 13.** Temperature histories used in the simulations for the two natural data sets. (A) Norwegian Continental Shelf data set. (B) Southeast Asia data set.

for the measured amount of illite, the simulated amount of illite may be less than the measured amount when the model does not predict a sufficient extent of the reaction. The modeled amount of illite may exceed the measured amount when (1) the modeled extent of illitization is extensive and the measured extent of feldspar dissolution and replacement by illite exceeds that required to account for measured illite volume or (2) the sample contains both kaolinite and K-feldspar reactants and the model predicts more extensive illite formation than has been measured for the sample. Unless stated otherwise, we use the same activation energy values for nucleation and growth and assume no activation energy benefit for nucleation on micaceous substrates. All simulations use an $A_g$ value of $-9 \times 10^{-12}$ mol/cm$^2$/s, an $A_n$ value of 8000 sites/cm$^2$/m.y., and an exclusion radius of 0.002 $\mu$m at 100°C (212°F) for fiber nucleation near existing crystallites. We adjusted quartz cementation kinetic and compaction model parameters for each sample to match the measured quartz cement and intergranular volumes, respectively. The purpose of this procedure is to provide the most accurate basis possible for reconstructing intergranular nucleation surface area.

## Norwegian Continental Shelf

The Haltenbanken region of offshore Norway is well suited for diagenetic studies because postdepositional rifting in this area has caused Jurassic sandstones with similar initial compositions and textures to have experienced a broad range in thermal exposures. Kaolinite and K-feldspar reactants show a marked decline in abundance at present-day temperatures greater than 120 to 130°C and cease to coexist at present-day temperatures in excess of 140°C (Bjørlykke et al., 1986; Ehrenberg and Nadeau, 1989; Chuhan et al. 2000, 2001). Authigenic illite, however, shows an inverse pattern of occurrence. Chuhan et al. (2000, 2001) concluded that the illitization reaction is mostly isochemical with respect to both K and Al based on their bulk chemical analysis of samples with a range in the extent of illitization. Formation-water analyses from this area have $K^+$ concentrations that do not exceed what would be expected for equilibrium with K-feldspar (Egeberg and Aagaard, 1989; Bjørlykke et al., 1995).

Simulation results indicate that apart from sample-specific input (i.e., composition, texture, and thermal history), a single set of input parameters accurately predicts the rapid transition from incipient to pervasive illitization with present-day temperature (Figure 14A) as well as the associated pattern of K-feldspar and kaolin-reactant abundances. These results were obtained with an activation energy of 73.2 kJ/mol for both crystal nucleation and growth. Simulations that use an activation energy value of 76 kJ/mol for these two parameters, however, systematically underpredict illite abundances for samples at temperatures less than 160°C (Figure 14A). By contrast, increased reaction rates

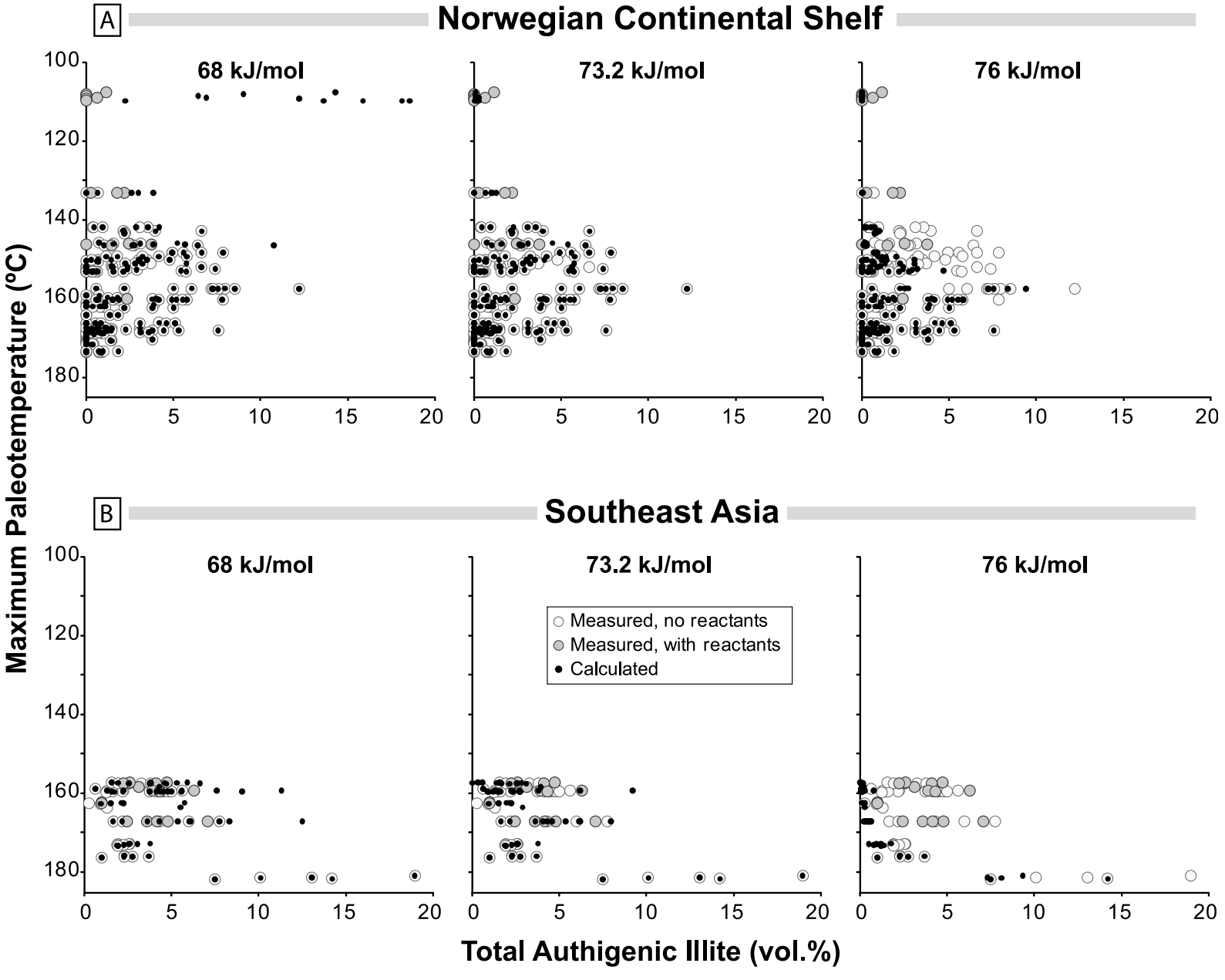


**Figure 14.** Comparison of the pattern in authigenic illite abundance with maximum temperature from petrographic data and with calculated values for the 68-, 73.2-, and 76-kJ/mol simulations described in the text. Sample measurements with reactants include both kaolin and K-feldspar, whereas samples lacking reactants may contain one of these two phases but not both.

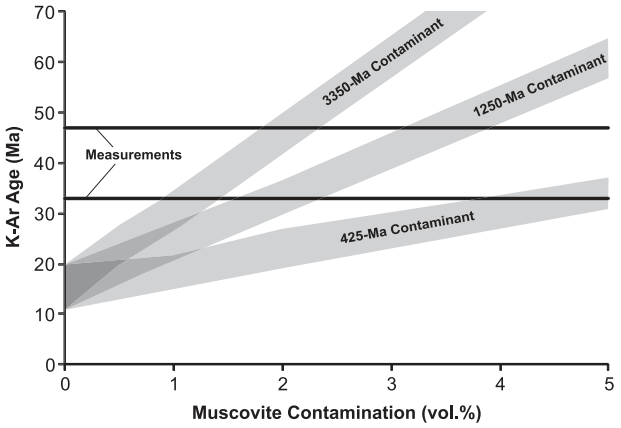


**Figure 15.** Impact of detrital contaminants on the simulated bulk K-Ar ages for five Garn Formation samples from a well in the Norwegian Continental Shelf data set using an activation energy of 73.2 kJ/mol. The horizontal lines indicate K-Ar measurements reported by Ehrenberg and Nadeau (1989) for two different Garn Formation samples in this well. The shaded regions indicate the range in simulated bulk K-Ar values for the five modeled samples as a function of the age and volume of a potential muscovite contaminant. The detrital contaminant ages used for the calculations are representative of values for Garn Formation zircons reported by Morton et al. (2009). Results indicate that only small amounts of Precambrian contaminants are required for the simulated results to be consistent with the measurements.

associated with activation energy values of 68 kJ/mol lead to simulated illite abundances that significantly overpredict measured values for cooler samples that have coexisting K-feldspar and kaolinite reactants (Figure 14A).

Although the simulation results are consistent with the present-day distribution of illite, fiber K-Ar ages provide an independent means to assess the veracity of the simulated timing of illite formation. Ehrenberg and Nadeau (1989) made K-Ar determinations on illite from 16 Garn Formation samples in 9 wells in the study area and obtained a range in values of 31 to 55 Ma. Of these wells, one overlaps with those in our data set and two samples analyzed from it have K-Ar ages of 33 and 47 Ma. The simulated K-Ar ages range from 11 to 20 Ma in the 73.2 kJ/mol run for pure, bulk authigenic illite for the five samples in our data set (Figure 15). Although the simulated ages are significantly younger than the measurements, Ehrenberg and Nadeau (1989) stated that their analyzed samples may have a problem with detrital contaminants. Recent U/Pb dating of detrital zircons in the Garn Formation shows ages ranging from approximately 400 to 3300 Ma (Morton et al., 2009). The potential effects of muscovite contaminants on the modeled K-Ar dates are shown as a function of the volume fraction of three representative ages of contaminants in Figure 15. The results indicate that as little as 1 to 3 vol.% of Proterozoic or Archean muscovite would result in K-Ar measurements that are consistent with model results. Even smaller contaminant volumes would be required to account for the K-Ar results if detrital K-feldspar of these ages were present due to the mineral's higher K content (Hamilton et al., 1989). The presence of such minor contaminants seems reasonable given that sandstones from this well in our data set contain K-feldspar (0 to 1 vol.%) and muscovite grains (0 to 0.7 vol.%) as well as clay matrix (0.7 to 3.7 vol.%), shale rock fragments (0.7 to 1.3 vol.%), and various other sedimentary, metamorphic, and plutonic rock fragments (1.7 to 3.6 vol.%) that contain these potential contaminants.

Although the 73.2-kJ/mol simulation predicts K-Ar ages that appear to be consistent with measurements, results from the other two simulations are not. The 76-kJ/mol simulation predicts only incipient illitization with K-Ar ages of around 6 Ma for the pure bulk sample. However, the simulated K-Ar ages for the 68-kJ/mol run range from 60 to 64 Ma for pure authigenic illite. In this case, even without contaminants, the simulated K-Ar ages are much too old to be consistent with the measurements. The 73.2-kJ/mol simulation thus provides the best fit to the illite abundance and pattern of occurrence and K-Ar ages.

This simulated timing for illitization is considerably older than some other workers have suggested for this region. Ehrenberg and Nadeau (1989) and Bjørlykke et al. (1995) proposed that the bulk of the illite formed during the past few million years based on the abrupt transition from incipient to pervasive illitization over present-day temperatures of 120 to 140°C (248 to 284°F) and a pulse of rapid burial during the Pliocene–Pleistocene. One line of evidence that supports older illitization consistent with our model results

is the considerable volume of quartz cement that postdates the initiation of fibrous illite nucleation and growth in sandstones from the study area. Bonnell et al. (1999) found illite fibers that were enveloped by up to 50 $\mu$m of quartz cement overgrowths in Viking Graben samples with similar burial histories. Using quartz cementation models with empirically calibrated kinetic parameters, Bonnell et al. (1999) concluded that it would have taken tens of millions of years to account for the volume of the quartz cement that encases the illite fibers.

## Southeast Asia

Like the NCS data set, the analyzed sandstones in the SEA data set were deposited in a prerift depositional system, and nearby formation-water $K^+$ concentrations do not exceed what would be expected from equilibrium with K-feldspar (Lundegard and Trevena, 1990). These sandstones, however, tend to be much richer in micaceous metamorphic rock fragments (Figure 12) and have experienced much greater heating rates compared to NCS samples (Figure 13). Despite these differences, the pattern of correspondence between calculated and measured illite abundances for the 68, 73.2, and 76 kJ/mol activation energy scenarios produces similar patterns (Figure 14B). Compared to the NCS simulations, however, the 68-kJ/mol simulation results in a much lower maximum extent of overprediction of illite abundance.

The clay minerals in this data set were analyzed rigorously by J. Reed Glasmann in an unpublished study (2001, personal communication) that incorporates K-Ar results in addition to optical thin-section petrography, whole rock and oriented clay x-ray diffraction (XRD), oxygen isotopic analysis, and SEM and TEM characterization. James Aronson conducted K-Ar analyses on the less than 0.2-$\mu$m equivalent settling diameter fraction-size separates made by Glasmann from four samples. Glasmann's XRD and TEM investigations indicate that K-feldspar and $2M_1$ polytype illite contaminants occur in coarser size fractions as well as one of the less than 0.2-$\mu$m fraction samples. Problems with detrital contamination are to be expected with these samples given the substantial abundances of micaceous and K-feldspar-bearing grains (mica grains: 0.3 to 5.2 vol.%, K-feldspar grains: 0 to 32.5 vol.%, metamorphic rock fragments: 2.0 to 42.5 vol.%, and plutonic rock fragments: 0 to 29.7 vol.%) as well as detrital clay (clasts: 0 to 6.1 vol.%, matrix: 0 to 5.0 vol.%). Thus, the measured K-Ar values likely represent a maximum integrated age for the authigenic illite, even for the less than 0.2-$\mu$m-size fraction samples that lack clear indications of detrital contamination.

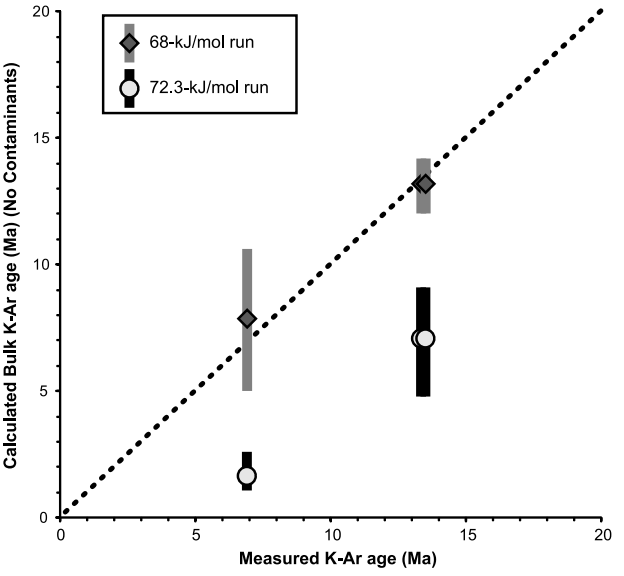


**Figure 16.** Correspondence between three measured K-Ar dates for the Southeast Asia data set (J. R. Glasmann, 2001, personal communication) and simulated values. The measurements were made on less than 0.2-$\mu$m equivalent settling diameter-size fractions. The two measurements with values of approximately 13 Ma are from different samples in the same well, and the 7-Ma value comes from a sample in a different well. Calculated results are shown for bulk, pure illite (no contaminants) for the 73.2- and 68-kJ/mol runs (the 76-kJ/mol run did not create sufficient illite to simulate K-Ar values). The calculated values are based on simulations for 10 samples from each well that are within a few meters of the sample with the K-Ar measurement. The symbol *y*-axis position shows the average calculated value, and the vertical bar shows the range in calculated values.

The simulated K-Ar dates for pure, bulk illite for the two wells with less than 0.2-$\mu$m fraction data without detected contaminants show a good correspondence with three measurements lacking obvious contamination, particularly for the 68-kJ/mol activation energy run (Figure 16). Although the

73.2-kJ/mol run results underpredict the measured values by 5 to 6 m.y. (Figure 16), this result seems reasonable given the likely detrital contamination problems discussed above.

### Natural Data Set Discussion

The illite model reproduces the present-day pattern of occurrence and abundances of illite, kaolin, and K-feldspar in both data sets. Moreover, simulation results made using the same kinetic parameters (73.2 kJ/mol) provide a good match to both data sets despite their large differences in geologic histories and grain compositions. Optimizing the activation energy independently for each data set resulted in only minor differences (73.4 and 73.0 kJ/mol, respectively, for the NCS and SEA data sets). By comparison, optimized activation energies for quartz precipitation of 60.7 and 55.5 kJ/mol, respectively, for the NCS and SEA data sets, show much larger differences (Lander et al., 2008).

The simulated K-Ar dates from the 73.2 kJ/mol runs also appear to be consistent with the measurements given their uncertainties. Additionally, the particle dimensions from these simulations are broadly consistent with Nagy's (1994) data from sandstones from the United Kingdom North Sea (Figure 17). The reconstructed depositional feldspar abundances for both data sets significantly exceed present-day abundances if we assume that Al and K are conserved on the thin-section scale and if we use illite and kaolin abundances for reference (Figure 12).

In these simulations, we assumed no activation energy benefit for nucleation on micaceous grains. Both data sets, however, contain micaceous grains, and they are especially abundant in metamorphic rock fragments in the SEA data set. We therefore ran simulations for a scenario where we assumed a 20-kJ/mol activation energy benefit for nucleating on micaceous surfaces compared to other surface types. After parameter optimization, this scenario has a slightly higher activation energy for crystal growth of 73.6 kJ/mol while having a comparable quality of fit to the data. Integrated times of illitization are slightly older (0.2 to 2.6 m.y. older on average, respectively, for SEA and NCS), and P50

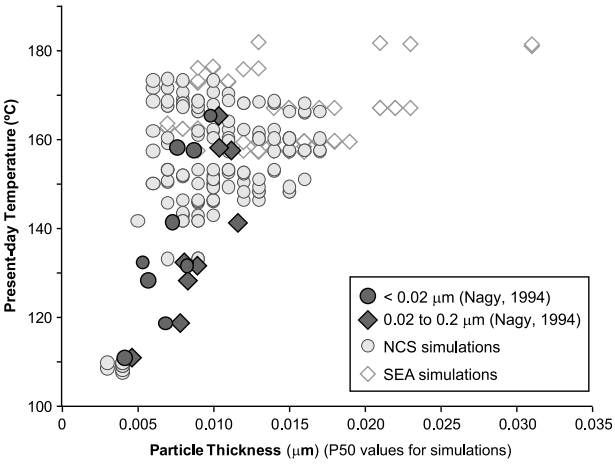


**Figure 17.** Comparison of average fibrous illite particle thicknesses reported by Nagy (1994) for two size separates (dark symbols) with simulated values for the two natural data sets using the 73.2-kJ/mol scenario (light symbols). The symbols for the simulation results indicate the predicted 50th percentile (P50) thickness value by crystallite count for each sample. The burial histories from the Norwegian Continental Shelf (NCS) data set are similar to those experienced by Nagy's (1994) samples, but the Southeast Asia (SEA) samples experienced much higher heating rates.

widths are somewhat smaller (by 12 to 19%, respectively, for NCS and SEA), but the results are otherwise similar. Thus, the model is relatively insensitive to an activation energy benefit for nucleation on micaceous grains as long as the kinetic parameters are optimized to match the measured pattern of illite occurrence.

## CONCLUSIONS

Our kinetic model for fibrous illite nucleation and growth reproduces the pattern in occurrence of fibrous illite as well as kaolin and K-feldspar reactants in two geologically distinct natural data sets using a single set of model parameters. Simulation results also appear to be at least broadly consistent with available K-Ar ages and data on illite fiber dimensions. We have shown that if this reaction is kinetically controlled, then the temperature range where illitization occurs will be a strong function of the thermal history. Therefore, the illitization process should not be expected to be a universal function of a simple temperature threshold of 120

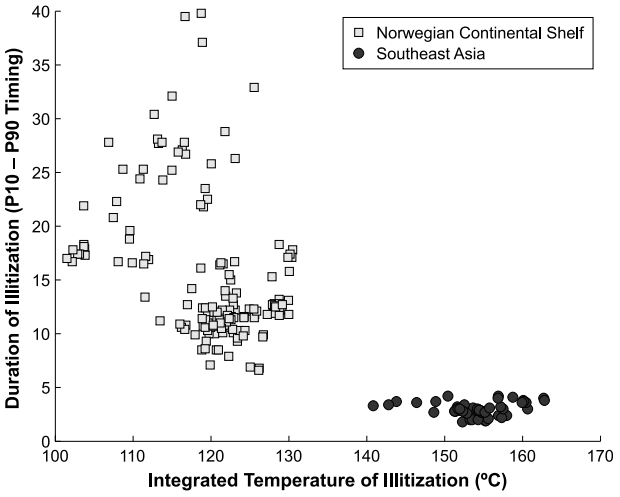


**Figure 18.** Comparison of the integrated temperature of illitization with the duration of illite formation for samples from the Norwegian Continental Shelf and Southeast Asia data sets using the 73.2-kJ/mol run scenario. The duration of illitization is based on the time span between the formation of the 10th and 90th volume percentiles, whereas the integrated temperature is the volume-weighted average temperature for illite formation. The much higher thermal exposures of the Southeast Asia data set have resulted in simulated illitization occurring at significantly faster rates and higher temperatures compared to Norwegian Continental Shelf samples.

to 140°C (248 to 284°F) as has been suggested by other workers (Ehrenberg and Nadeau, 1989; Bjørlykke et al., 1995; Bjørlykke, 1998). This kinetic behavior is well illustrated by the tendency for the simulations of NCS samples to have cooler integrated temperatures of formation and longer durations of illitization than SEA samples that have been exposed to far greater heating rates (Figure 18).

Model sensitivity tests indicate greatly accelerated rates of illitization in the presence of potassic brines. Results for a synthetic Jurassic-aged sample show a dramatic drop from 135 to 80°C (275 to 176°F) in the paleotemperature of pervasive illitization when $K^+$ activity increases from levels expected for equilibrium with K-feldspar to that associated with fluid inclusions in naturally occurring halite. Sensitivity tests also predict that otherwise similar sandstones with comparable maximum temperatures but longer thermal residence times are illitized at lower temperatures and at slower overall rates and that completion of the reaction takes longer in sandstones with more reactants but similar thermal exposures.

## REFERENCES CITED


Aagaard, P., J. S. Jahren, and P. K. Egeberg, 1992, North Sea clastic diagenesis and formation water constraints, *in* Y. K. Kharaka and A. S. Maest, eds., Water-rock interaction: Proceedings of the 7th International Symposium, Park City, Utah, July 13–18.

Altaner, S. P., 1986, Comparison of rates of smectite illitization with rates of K-feldspar dissolution: Clays and Clay Minerals, v. 34, p. 608–611, doi:10.1346/CCMN.1986.0340517.

Bazin, B., É. Brosse, and F. Sommer, 1997a, Chemistry of oilfield brines in relation to diagenesis of reservoirs: 1. Use of mineral stability fields to reconstruct in situ water composition. Example of the Mahakam Basin: Marine and Petroleum Geology, v. 14, p. 481–495, doi:10.1016/S0264-8172(97)00004-4.

Bazin, B., É. Brosse, and F. Sommer, 1997b, Chemistry of oilfield brines in relation to diagenesis of reservoirs: 2. Reconstruction of paleo-water composition for modeling illite diagenesis in the Greater Alwyn area (North Sea): Marine and Petroleum Geology, v. 14, p. 497–511, doi:10.1016/S0264-8172(97)00005-6.

Berger, G., J. C. Lacharpagne, B. Velde, D. Beaufort, and B. Lanson, 1997, Kinetic constraints on illitization reactions and the effects of organic diagenesis in sandstone/shale sequences: Applied Geochemistry, v. 12, p. 23–35, doi:10.1016/S0883-2927(96)00051-0.

Bethke, C. M., 1996, Geochemical reaction modeling—Concepts and applications: New York, Oxford University Press, 397 p.

Bjørkum, P. A., and N. Gjelsvik, 1988, An isochemical model for formation of authigenic kaolinite, K-feldspar and illite in sediments: Journal of Sedimentary Petrology, v. 58, p. 506–511.

Bjørlykke, K., 1998, Clay mineral diagenesis in sedimentary basins—A key to the prediction of rock properties. Examples from the North Sea Basin: Clay Minerals, v. 33, p. 15–34, doi:10.1180/000985598545390.

Bjørlykke, K., P. Aagaard, H. Dypvik, D. S. Hastings, and A. S. Harper, 1986, Diagenesis and reservoir properties of Jurassic sandstones from the Haltenbanken area, offshore mid Norway, *in* A. M. Spencer, ed., Petroleum geology of the Northern European margin: Norwegian Petroleum Society, London, Graham and Trotman, p. 285–292.

Bjørlykke, K., T. Nedkvitne, M. Ramm, and G. C. Saigal, 1992, Diagenetic processes in the Brent group, *in* A. C. Morton, R. S. Haszeldine, M. R. Giles, and S. Brown, eds., Geology of the Brent Group: Geological Society (London) Special Publication 61, p. 263–288.

Bjørlykke, K., P. Aagaard, P. K. Egeberg, and S. P. Simmons, 1995, Geochemical constraints from formation water analyses from the North Sea and the Gulf Coast basins on quartz, feldspar and illite precipitation in reservoir rocks, *in* J. M. Cubitt and W. A. England, eds., The geochemistry of reservoirs: Geological Society (London) Special Publication 86, p. 33–50.

Blum, A. E., and L. L. Stillings, 1995, Feldspar dissolution kinetics, *in* A. F. White and S. L. Brantley, eds., Chemical weathering rates of silicate minerals, v. 31, p. 291–346.

Bonnell, L. M., C. J. Lowrey, and A. A. Bray, 1999, The timing of illitization, Haltenbanken, mid-Norway (abs.): AAPG Annual Meeting Program with Abstracts, v. 8, p. A14.

Bove, D. J., D. D. Eberl, D. K. McCarty, and G. P. Meeker, 2002, Characterization and modeling of illite crystal particles and growth mechanisms in a zoned hydrothermal deposit, Lake City, Colorado: American Mineralogist, v. 87, p. 1546–1556.

Brosse, E., J. Matthews, B. Baxin, Y. Le Gallo, and F. Sommer, 2000, Related quartz and illite cementation in the Brent sandstones: A modeling approach, *in* R. H. Worden and S. Morad, eds., Quartz cementation in sandstones: International Association of Sedimentologists Special Publication 29, p. 51–66.

Canals, M., and J. D. Meunier, 1995, A model for porosity reduction in quartzite reservoirs by quartz cementation: Geochimica et Cosmochimica Acta, v. 59, p. 699–709, doi:10.1016/0016-7037(94)00355-P.

Cendón, D. I., C. Ayora, J. J. Pueyo, and C. Taberner, 2003, The geochemical evolution of the Catalan potash subbasin, South Pyrenean foreland basin (Spain): Chemical Geology, v. 200, p. 339–357, doi:10.1016/S0009-2541(03)00195-5.

Chermak, J. A., and J. D. Rimstidt, 1990, The hydrothermal transformation of kaolinite to muscovite/illite: Geochimica et Cosmochimica Acta, v. 54, p. 2979–2990, doi:10.1016/0016-7037(90)90115-2.

Chuhan, F. A., K. Bjørlykke, and C. Lowrey, 2000, The role of provenance in illitization of deeply buried reservoir sandstones from Haltenbanken and north Viking Graben, offshore Norway: Marine and Petroleum Geology, v. 17, p. 673–689.

Chuhan, F. A., K. Bjørlykke, and C. J. Lowrey, 2001, Closed-system burial diagenesis in reservoir sandstones: Examples from the Garn Formation at Haltenbanken area, offshore mid-Norway: Journal of Sedimentary Research, v. 71, p. 15–26, doi:10.1306/041100710015.

Clauer, N., and S. Chaudhuri, 1995, Clays in crustal environment: Isotope dating and tracing: Heidelberg, Springer, 359 p.

Clauer, N., J. D. Cocker, and S. Chaudhuri, 1992, Isotopic dating of diagenetic illites in reservoir sandstones: Influence of the investigator effect: SEPM (Society for Sedimentary Geology), v. 47, p. 5–12.

Clauer, N., N. Liewig, B. Ledesert, and H. Zwingmann, 2008, Thermal history of Triassic sandstones from the Vosges Mountains-Rhine Graben rifting area, NE France, based on K-Ar illite dating: Clay Minerals, v. 43, p. 363–379, doi:10.1180/claymin.2008.043.3.03.

Cocker, J. D., 1986, Authigenic illite morphology: Appearances can be deceiving: AAPG Bulletin, v. 70, p. 575.

Deer, W. A., R. A. Howie, and J. Zussman, 1966, Introduction to the rock-forming minerals: London, Longman, 528 p.

De Ros, L. F., 1998, Heterogeneous generation and evolution of diagenetic quartarenites in the Silurian–Devonian Furnas Formation of the Paraná Basin, southern Brazil: Sedimentary Geology, v. 116, p. 99–129, doi:10.1016/S0037-0738(97)00081-X.

Eberl, D. D., V. A. Drits, and J. Środoń, 1998, Deducing growth mechanisms for minerals from the shapes of crystal size distributions: American Journal of Science, v. 298, p. 499–533.

Egeberg, P. K., and P. Aagaard, 1989, Origin and evolution of formation waters from oil fields on the Norwegian Shelf: Applied Geochemistry, v. 4, p. 131–142, doi:10.1016/0883-2927(89)90044-9.

Ehrenberg, S. N., and P. H. Nadeau, 1989, Formation of diagenetic illite in sandstones of the Garn Formation, Haltenbanken area, mid-Norwegian Continental Shelf: Clay Minerals, v. 24, p. 233–253, doi:10.1180/claymin.1989.024.2.09.

Folk, R. L., 1980, Petrology of sedimentary rocks: Austin, Texas, Hemphill Publishing Company, 184 p.

Franks, S. G., and H. Zwingmann, 2010, Origin and timing of late diagenetic illite in the Permian–Carboniferous Unayzah sandstone reservoirs of Saudi Arabia: AAPG Bulletin, v. 94, p. 1133–1159, doi:10.1306/04211009142.

Gaupp, R., A. Matter, J. Platt, K. Ramseyer, and J. Walzebuck, 1993, Diagenesis and fluid evolution of deeply buried Permian (Rotliegende) gas reservoirs, northwest Germany: AAPG Bulletin, v. 77, p. 1111–1128.

Girard, J. P., I. A. Munz, H. Johansen, J. C. Lacharpagne, and F. Sommer, 2002, Diagenesis of the Hild Brent sandstones, northern North Sea: Isotopic evidence for the prevailing influence of deep basinal water: Journal of Sedimentary Research, v. 72, p. 746–759, doi:10.1306/040102720746.

Glasmann, J. R., 1992, The fate of feldspar in Brent Group reservoirs, North Sea: A regional synthesis of diagenesis in shallow, intermediate, and deep burial environments, *in* A. C. Morton, R. S. Haszeldine, M. R. Giles, and S. Brown, eds., Geology of the Brent Group: Geological Society (London) Special Publication 61, p. 329–350.

Glasmann, J. R., P. D. Lundegard, R. A. Clark, B. K. Penny, and I. D. Collins, 1989, Geochemical evidence for the history of diagenesis and fluid migration: Brent sandstone, Heather field, North Sea: Clay Minerals, v. 24, p. 255–284, doi:10.1180/claymin.1989.024.2.10.

Güven, N., 2001, Mica structure and fibrous growth of illite: Clays and Clay Minerals, v. 49, p. 189–196, doi:10.1346/CCMN.2001.0490301.

Güven, N., W. F. Hower, and D. K. Davies, 1980, Nature of authigenic illites in sandstone reservoirs: Journal of Sedimentary Petrology, v. 50, p. 761–766.

Hamilton, P. J., S. Kelley, and A. E. Fallick, 1989, K-Ar dating of illite in hydrocarbon reservoirs: Clay Minerals, v. 24, p. 215–232, doi:10.1180/claymin.1989.024.2.08.

Hamilton, P. J., M. R. Giles, and P. Ainsworth, 1992, K-Ar dating of illites in Brent Group reservoirs: A regional perspective, *in* A. Morton, R. Haszeldine, M. Giles, and S. Brown, eds., Geology of the Brent Group: Geological Society (London) Special Publication 61, p. 377–400.

Hunziker, J. C., 1986, The evolution of illite to muscovite: An example of the behavior of isotopes in low-grade metamorphic terrains: Chemical Geology, v. 57, p. 31–40, doi:10.1016/0009-2541(86)90092-6.

Hutcheon, I., M. Shevalier, and H. J. Abercrombie, 1993, pH buffering by metastable mineral-fluid equilibria

and evolution of carbon dioxide fugacity during burial diagenesis: Geochimica et Cosmochimica Acta, v. 54, p. 1017–1027, doi:10.1016/0016-7037(93)90037-W.
Jahren, J. S., and P. Aagaard, 1989, Compositional variations in diagenetic chlorites and illites, and relationships with formation-water chemistry: Clay Minerals, v. 24, p. 157–170, doi:10.1180/claymin.1989.024.2.04.
Kantorowicz, J., 1984, The nature, origin and distribution of authigenic clay minerals, from Middle Jurassic Ravenscar and Brent Group sandstones: Clay Minerals, v. 19, p. 359–375, doi:10.1180/claymin.1984.019.3.08.
Kantorowicz, J. D., 1990, The influence of variations in illite morphology on the permeability of Middle Jurassic Brent Group sandstones, Cormorant field, U.K. North Sea: Marine Petroleum Geology, v. 7, p. 66–74, doi:10.1016/0264-8172(90)90057-N.
Kharaka, Y. K., R. W. Hull, and W. W. Carothers, 1985, Water-rock interactions in sedimentary basins, *in* D. L Gautier, Y. K. Kharaka, and R. C. Surdam, eds., Role of organic matter in sediment diagenesis: SEPM Short Course 17, p. 79–176.
Kittel, C., and H. Kroemer, 1980, Thermal physics: New York, Freeman, 473 p.
Lander, R. H., S. Bloch, S. Mehta, and C. D. Atkinson, 1990, Burial diagenesis of paleosols in the Giant Yacheng Gas field, People's Republic of China: Bearing on illite reaction pathways: Journal of Sedimentary Research, v. 61, p. 256–268.
Lander, R. H., R. E. Larese, and L. M. Bonnell, 2008, Toward more accurate quartz cement models: The importance of euhedral versus noneuhedral growth rates: AAPG Bulletin, v. 92, p. 1537–1563, doi:10.1306/07160808037.
Lanson, B., D. Beaufort, G. Berger, J. Baradat, and J. C. Lacharpagne, 1996, Illitization of diagenetic kaolinite-to-dickite conversion series: Late-stage diagenesis of the Lower Permian Rotliegende sandstone reservoir, offshore of the Netherlands: Journal of Sedimentary Research, v. 66, p. 501–518.
Lanson, B., D. Beaufort, G. Berger, A. Bauer, A. Cassagnabère, and A. Meunier, 2002, Authigenic kaolin and illitic minerals during burial diagenesis of sandstones: A review: Clay Minerals, v. 37, p. 1–22, doi:10.1180/0009855023710014.
Lasaga, A. C., 1998, Kinetic theory in the earth sciences: Princeton series in geochemistry: Princeton, New Jersey, Princeton University Press, 811 p.
Lee, M., 1984, Diagenesis of the Permian Rotliegendes sandstone, North Sea: K-Ar, $^{18}0/^{16}O$ and petrographic evidence: Ph.D. thesis, Case Western Reserve University, Cleveland, Ohio, 362 p.
Lee, M., J. L. Aronson, and S. M. Savin, 1985, K/Ar dating of Rotliegendes sandstone, Netherlands: AAPG Bulletin, v. 68, p. 1381–1385.
Lee, M., J. L. Aronson, and S. M. Savin, 1989, Timing and conditions of Permian Rotliegendes sandstone diagenesis, southern North Sea: K/Ar and oxygen isotope data: AAPG Bulletin, v. 73, p. 195–215.
Lichtner, P. C., 1988, The quasi-stationary state approximation to coupled mass transport and fluid-rock interaction in a porous medium: Geochimica et Cosmochimica Acta, v. 52, p. 143–165, doi:10.1016/0016-7037(88)90063-4.
Lundegard, P. D., and A. S. Trevena, 1990, Sandstone diagenesis in the Pattani Basin (Gulf of Thailand): History of water-rock interaction and comparison with the Gulf of Mexico: Applied Geochemistry, v. 5, p. 669–685, doi:10.1016/0883-2927(90)90064-C.
Macchi, L., C. D. Curtis, A. Levison, K. Woodward, and C. R. Hughes, 1990, Chemistry, morphology, and distribution of illites from Morecambe gas field, Irish Sea, offshore United Kingdom: AAPG Bulletin, v. 74, p. 296–308.
Maher, K., C. I. Steefel, D. J. DePaolo, and B. E. Viani, 2006, The mineral dissolution rate conundrum: Insights from reactive transport modeling of U isotopes and pore fluid chemistry in marine sediments: Geochimica et Cosmochimica Acta, v. 70, p. 337–363, doi:10.1016/j.gca.2005.09.001.
Matthews, J. C., B. Velde, and H. Johansen, 1994, Significance of K-Ar ages of authigenic illitic clay-minerals in sandstones and shales from the North Sea: Clay Minerals, v. 29, p. 379–389, doi:10.1180/claymin.1994.029.3.09.
McHardy, W. J., M. J. Wilson, and J. M. Tait, 1982, Electron microscope and x-ray diffraction studies of filamentous illitic clay from sandstones of the Magnus field: Clay Minerals, v. 17, p. 23–29, doi:10.1180/claymin.1982.017.1.04.
Merino, E., P. Ortoleva, and P. Strickholm, 1983, Generation of evenly spaced pressure-solution seams during (late) diagenesis: A kinetic theory: Contributions to Mineralogy and Petrology, v. 82, p. 360–370
Meunier, A., 2006, Why are clay minerals small?: Clay Minerals, v. 41, p. 551–566, doi:10.1180/0009855064120205.
Meunier, A., B. Velde, and P. Zalba, 2004, Illite K-Ar dating and crystal growth processes in diagenetic environments: A critical review: Terra Nova, v. 16, p. 296–304, doi:10.1111/j.1365-3121.2004.00563.x.
Midtbø, R. E. A., J. M. Rykkje, and M. Ramm, 2000, Deep burial diagenesis and reservoir quality along the eastern flank of the Viking Graben. Evidence for illitization and quartz cementation after hydrocarbon emplacement: Clay Minerals, v. 35, p. 227–237, doi:10.1180/000985500546602.
Morton, A., C. Hallsworth, D. Strogen, A. Whitham, and M. Fanning, 2009, Evolution of provenance in the NE Atlantic rift: The Early–Middle Jurassic succession in the Heidrun field, Halten Terrace, offshore Mid-Norway: Marine and Petroleum Geology, v. 26, p. 1100–1117, doi:10.1016/j.marpetgeo.2008.07.006.
Morton, R. A., and L. S. Land, 1987, Regional variations in formation water chemistry, Frio Formation (Oligocene), Texas Gulf Coast: AAPG Bulletin, v. 71, p. 191–206.
Nadeau, P. H., and A. Hurst, 1991, Application of backscattered electron microscopy to the quantification of clay mineral microporosity in sandstones: Journal of Sedimentary Research, v. 61, p. 921–925.
Nagy, K. L., 1994, Application of morphological data obtained using scanning force microscopy to quantification of fibrous illite growth rates, *in* K. L. Nagy and A. E Blum, eds., Scanning probe microscopy of clay minerals: CMS Workshop Lectures, Bloomington, Indiana, The Clay Minerals Society, v. 7, p. 204–239.

Oelkers, E. H., P. A. Bjørkum, O. Walderhaug, N. H. Nadeau, and W. M. Murphy, 2000, Making diagenesis obey thermodynamics and kinetics: The case of quartz cementation in sandstones from offshore mid-Norway: Applied Geochemistry, v. 15, p. 295–309, doi:10.1016/S0883-2927(99)00047-5.

Palandri, J. L., and M. H. Reed, 2001, Reconstruction of in situ composition of sedimentary formation waters: Geochimica et Cosmochimica Acta, v. 65, p. 1741–1767, doi:10.1016/S0016-7037(01)00555-5.

Pallatt, N. M., M. J. Wilson, and W. J. McHardy, 1984, The relationship between permeability and the morphology of diagenetic illite in reservoir rocks: Journal of Petroleum Technology, v. 36, p. 2225–2227.

Panda, M. N., and L. W. Lake, 1995, A physical model of cementation and its effects on single-phase permeability: AAPG Bulletin, v. 79, p. 431–443.

Pevear, D. R., 1999, Illite and hydrocarbon exploration: Proceedings of the National Academy of Science, U.S.A., v. 96, p. 3440–3446.

Ramm, M., and A. E. Ryseth, 1996, Reservoir quality and burial diagenesis in the Statfjord Formation, North Sea: Petroleum Geoscience, v. 2, p. 313–324.

Robinson, A. G., M. L. Coleman, and J. G. Gluyas, 1993, The age of illite cement growth, Village fields area, southern North Sea: Evidence from K-Ar ages and $^{18}O/^{16}O$ ratios: AAPG Bulletin, v. 77, p. 68–80.

Rossel, N. C., 1982, Clay mineral diagenesis in Rotliegend eolian sandstones of the southern North Sea: Clay Minerals, v. 17, p. 69–77, doi:10.1180/claymin.1982.017.1.07.

Środoń, J., and D. D. Eberl, 1984, Illite, *in* S. W. Bailey, ed., Micas: Reviews in Mineralogy, v. 13, p. 495–544.

Środoń, J., D. D. Eberl, and V. A. Drits, 2000, Evolution of fundamental-particle size during illitization of smectite and implications for reaction mechanism: Clays and Clay Minerals, v. 48, p. 446–458, doi:10.1346/CCMN.2000.0480405.

Środoń, J., N. Clauer, and D. D. Eberl, 2002, Interpretation of K-Ar dates of illitic clays from sedimentary rocks aided by modeling: American Mineralogist, v. 87, p. 1528–1535.

Stalder, P. J., 1973, Influence of crystallographic habit and aggregate structure of authigenic clay minerals on sandstone permeability: Geologie en Mijnbouw, v. 53, p. 217–220.

Steiger, R. H., and E. Jäger, 1977, Subcommission on Geochronology: Convention on the use on decay constants in geo- and cosmochronology: Earth and Planetary Science Letters, v. 36, p. 359–362, doi:10.1016/0012-821X(77)90060-7.

Stroker, T., and N. Harris, 2009, K-Ar dating of authigenic illites: Integrating diagenetic history of the Mesa Verde Group, Piceance Basin, NW Colorado (abs.): AAPG Annual Meeting Abstracts, v. 18, p. 206.

Szczerba, M., and J. Środoń, 2009, Extraction of diagenetic and detrital ages of the $^{40}K_{detrital}/^{40}K_{diagenetic}$ ratio from K-Ar dates of clay fractions: Clays and Clay Minerals, v. 57, p. 93–103, doi:10.1346/CCMN.2009.0570109.

Thyne, G., B. P. Boudreau, M. Ramm, and R. E. Midtbø, 2001, Simulation of potassium feldspar dissolution and illitization in the Statfjord Formation, North Sea: AAPG Bulletin, v. 85, p. 621–635.

Walderhaug, O., 1994, Precipitation rates for quartz cement in sandstones determined by fluid-inclusion microthermometry and temperature-history modeling: Journal of Sedimentary Research, v. A64, p. 324–333.

Walderhaug, O., 1996, Kinetic modeling of quartz cementation and porosity loss in deeply buried sandstone reservoirs: AAPG Bulletin, v. 80, p. 731–745.

Walderhaug, O., 2000, Modeling quartz cementation and porosity loss in Middle Jurassic Brent Group sandstones of the Kvitebjørn field, northern North Sea: AAPG Bulletin, v. 84, p. 1325–1339.

Walderhaug, O., and P. A. Bjørkum, 1998, Calcite cement in shallow marine sandstones: growth mechanisms and geometry, *in* S. Morad, ed., Carbonate cementation in sandstones: Distribution patterns and geochemical evolution: International Association of Sedimentologists Special Publication 26, p. 179–192.

White, A. F., and S. L. Brantley, 2003, The effect of time on the weathering of silicate minerals: Why do weathering rates in the laboratory and field?: Chemical Geology, v. 202, p. 479–506, doi:10.1016/j.chemgeo.2003.03.001.

Wilkinson, M., and R. S. Haszeldine, 2002a, Fibrous illite in oilfield sandstones—A nucleation kinetic theory of growth: Terra Nova, v. 14, p. 56–60, doi:10.1046/j.1365-3121.2002.00388.x.

Wilkinson, M., and R. S. Haszeldine, 2002b, Problems with argon: K-Ar ages in Gulf Coast shales: Chemical Geology, v. 191, p. 277–283, doi:10.1016/S0009-2541(02)00145-6.

Worden, R. H., and S. Morad, 2000, Quartz cementation in oil field sandstones: A review of the key controversies, *in* R. H. Worden and S. Morad, eds., Quartz cementation in sandstones: International Association of Sedimentologists Special Publication 29, p. 1–20.

Ylagan, R. F., D. R. Pevear, and P. J. Vrolijk, 2000, Discussion of "Extracting K-Ar ages from shales: A theoretical test": Clay Minerals, v. 35, p. 599–604, doi:10.1180/000985500546918.

Zhu, C., 2005, In situ feldspar dissolution rates in an aquifer: Geochimica et Cosmochimica Acta, v. 69, p. 1435–1453, doi:10.1016/j.gca.2004.09.005.

Zwingmann, H., N. Clauer, and R. Gaupp, 1998, Timing of fluid flow in a sandstone reservoir of the North German Rotliegend (Permian) by K-Ar dating of related hydrothermal illite, *in* J. Parnell, ed., Dating and duration of fluid flow and fluid-rock interaction: Geological Society (London) Special Publication 144, p. 91–106.

Zwingmann, H., N. Clauer, and R. Gaupp, 1999, Structure-related geochemical (REE) and isotopic (K-Ar, Rb-Sr, $\delta^{18}O$) characteristics of clay minerals from Rotliegend sandstone reservoirs (Permian, northern Germany): Geochimica et Cosmochimica Acta, v. 63, p. 2805–2823, doi:10.1016/S0016-7037(99)00198-2.